An advanced elastoplastic framework accounting for induced plastic anisotropy fully coupled with ductile damage

Joseph Paux, Mohamed Ben Bettaieb, Houssem Badreddine, Farid Abed-Meraim, Carl Labergere, Khemais Saanouni

▶ **To cite this version:**

Joseph Paux, Mohamed Ben Bettaieb, Houssem Badreddine, Farid Abed-Meraim, Carl Labergere, et al.. An advanced elastoplastic framework accounting for induced plastic anisotropy fully coupled with ductile damage. International Journal of Mechanical Sciences, 2021, 207, pp.106620. 10.1016/j.ijmecsci.2021.106620 . hal-03276459

HAL Id: hal-03276459
https://hal.science/hal-03276459v1

Submitted on 2 Jul 2021

HAL is a multi-disciplinary open access archive for the deposit and dissemination of scientific research documents, whether they are published or not. The documents may come from teaching and research institutions in France or abroad, or from public or private research centers.

L'archive ouverte pluridisciplinaire **HAL**, est destinée au dépôt et à la diffusion de documents scientifiques de niveau recherche, publiés ou non, émanant des établissements d'enseignement et de recherche français ou étrangers, des laboratoires publics ou privés.

An advanced elastoplastic framework accounting for induced plastic anisotropy fully coupled with ductile damage

J. Paux[1,2,3,4], M. Ben Bettaieb[2], H. Badreddine[3,*], F. Abed-Meraim[2], C. Labergere[3], K. Saanouni[3]

[1] IRT M2P, 4 rue Augustin Fresnel, F-57070 Metz, France

[2] Arts et Métiers Institute of Technology, CNRS, Université de Lorraine, LEM3, F-57000, Metz, France

[3] ICD/LASMIS, University of Technology of Troyes, UMR 6281, CNRS, Troyes, France

[4] ITheMM - EA 7548, University of Reims Champagne Ardenne, Charleville Mézières, France

Abstract

We present in this investigation an advanced phenomenological approach combining the computational efficiency of classical phenomenological plasticity models and the accuracy and high resolution of multiscale crystal plasticity schemes. Within this advanced approach, a new phenomenological constitutive framework has been developed and implemented into ABAQUS/Standard finite element (FE) code. Compared to classical approaches, this framework allows accounting for initial and induced plastic anisotropy, isotropic nonlinear hardening and the full coupling with isotropic ductile damage. Material parameters corresponding to this phenomenological constitutive framework are identified based on multiscale polycrystalline simulations, where the self-consistent scheme is used to ensure the transition between the single crystal and polycrystal scales. The single crystal mechanical behavior is assumed to be elastoplastic (rate-independent), and microscopic material degradation is well-considered by introducing a scalar damage variable at each crystallographic slip system for each individual grain. The evolution of polycrystalline yield surfaces induced by the evolution of crystallographic texture, is accurately reproduced by the new constitutive modeling, where the anisotropy parameters are assumed to evolve during plastic deformation. Their evolution laws are identified based on multiscale simulations. The different identification procedures are presented and extensively discussed. The robustness and reliability of this advanced model are

[*] Email address of the corresponding author: Houssem.Badreddine@utt.fr

analyzed through some relevant numerical predictions obtained by applying a combined tensile/shear test.

Keywords: plasticity, damage, full coupling, induced plastic anisotropy, phenomenological models, multiscale schemes.

1. Introduction

Finite element (FE) simulations have become a powerful tool in the modeling of metal structures and components during sheet metal forming processes. The efficiency and reliability of FE modeling depend not only on the numerical strategies and methods used to perform these simulations (size, type, and number of finite elements, algorithms to integrate the constitutive equations, numerical techniques to solve the balance equations, …), but also on the choice of the constitutive framework able to accurately reproduce the real mechanical response. Classically, constitutive models may be broadly classified into two main categories: macroscopic phenomenological approaches and micro-macro multiscale models.

Currently, macroscopic phenomenological approaches are the most widely used to numerically simulate sheet forming processes. These approaches can be classified into two main classes. The first and simplest one includes conventional plasticity models associating an isotropic hardening rule with a yield function using an enhanced definition of equivalent stress. Within these models, isotropic hardening is described by a scalar function non-linearly dependent on the accumulated plastic strain. In this case, attention is focused only on the form of the equivalent stress to describe the initial as well as induced plastic anisotropies using quadratic [1] or non-quadratic [2–7] equivalent stress measures, while the 'center' of the yield function remains fixed in the stress space (i.e. no kinematic hardening is considered). As well admitted, this class of models is unable to accurately predict the stress state of the material subjected to large plastic strains under complex non-monotonic and non-proportional loading paths. To overcome this limitation, many authors have proposed several extensions of this kind of models to account for scalar distortional hardening using associated flow rules [8–11] and non-associated flow rules [11–15]. Yield surface distortion is then described by anisotropic hardening leading to a significant change in the shape of the yield locus as the hardening increases. More recent investigations tend to describe the yield surface distortion by an internal structure tensor in the yield stress, using the so-called Homogeneous Anisotropic Hardening (HAH) concept, which is based on homogeneous yield functions/plastic potentials combining a stable, isotropic hardening-type component and a fluctuating component [16–18].

The second strategy, which is more advanced than the first one, is based on the framework of the thermodynamics of irreversible processes. It consists in defining several pairs of state variables associated with the different physical phenomena to be taken into consideration. Various physical phenomena characterized by strong interactions (or full coupling) with highly nonlinear evolutions, such as mixed isotropic, kinematic, distortional hardening and, different damage kinds (ductile, creep, fatigue, …) can be considered. The state and dissipation potentials as well as the yield functions are then taken as a convex functions of these state variables in order to derive a complete set of fully coupled thermodynamically-consistent constitutive equations [19–23]. Advanced metallic materials exhibit various strong initial and induced anisotropies (see for example [11]), which cannot be described by a simple associated plasticity theory with a single yield function with different sources of anisotropies under concern. François [24] has proposed a new yield criterion in which a distortion deviatoric stress tensor including kinematic hardening is used instead of the classical deviatoric stress tensor defining an egg shaped yield surface. The François' model has been extended in [25] to take into account the effect of orthogonal loading evolution in the framework of non-associated plasticity. Some other proposed models have been introduced through variations in fourth-rank anisotropy tensor of the yield function [26–28]. Using similar approach, a thermodynamically-consistent framework of isotropic, kinematic and distortional hardening under small plastic strains has been developed in [29].

Otherwise, for metal forming processes, the material is subjected to large plastic strains inducing flow localization in narrow shear bands, where some micro-voids and micro-cracks are expected to appear leading to ductile damage initiation and propagation. Accordingly, ductile damage and its full effects on the other phenomena (strong coupling) are then necessary to take into account accurately predict the stress state and the plastic flow during metal forming. Several theories have been proposed to describe this damage occurrence as well as its effect on the material behavior. The most widely used approach in metal forming is based on the continuum damage mechanics, which represents the ductile damage by scalar or tensor state variables [20, 22, 30–35], and its effect on the material behavior is accounted for thanks to the equivalence assumptions (strain equivalence, stress equivalence or energy equivalence).

These phenomenological approaches have the advantage of being simpler to implement in FE environment and consume relatively low CPU time, even for complex models, compared to the multiscale micro-macro models. However, the development of new high performance materials (like High Strength Steels, High Strength Aluminum, Magnesium alloys) induces, due to their complex microstructures, more and more complex phenomena that shall be taken into account in models, thus leading to an increase of the number of material parameters [21, 23, 36–39]. This leads to increasing significantly of the number of material parameters and constitutes the main drawback of this approach,

because their identification requires a large number of experimental mechanical tests. Furthermore, due to the technical limitations of the current experimental devises, it is always very difficult and sometimes unrealizable to characterize all the complex phenomena affecting the material behavior (initial and induced anisotropy, distortion of the yield surface, transient and permanent hardening, ductile damage, …) in six-dimensional stress or strain spaces by classical mechanical testing on thin sheet metals.

The above-mentioned inherent limitations of macroscopic phenomenological approaches opened the way towards the development of polycrystalline multiscale models. Contrarily to the phenomenological approaches, multiscale schemes allow explicitly linking the macroscopic behavior to microscopic mechanisms and phenomena such as the evolution of crystallographic and morphologic textures, the dislocations motion, the slip on the crystallographic slip systems... This feature constitutes the main advantage of multiscale approaches compared to phenomenological ones. Consequently, these multiscale approaches have been widely coupled with the FEM to simulate sheet metal forming processes. From a practical point of view, to perform such simulations, the sheet metal is discretized with a large number of finite elements and a polycrystalline aggregate, made of a sufficient number of grains to be representative of the studied material, is associated with each integration point. In the literature, several multiscale schemes have been developed and used to ensure the transition between the grain and polycrystal scales. These schemes can be classified into two main families, namely the mean-fields and the full-fields homogenization approaches. Mean-field approaches have been initiated by the well-known Taylor model [40–42]. This model assumes that the strain field is homogeneous through the polycrystalline aggregate. It has been coupled in several contributions [43–45] with the FE method to simulate different forming processes. In reality, the assumption of the strain field homogeneity cannot be fulfilled due to the grain boundaries and the differences observed in the crystallographic orientation between the different grains or crystals. Moreover, the microscopic equilibrium condition across the grain boundaries is not ensured when the Taylor model is used. These violations generally lead to some inaccuracies in the FE predictions compared to experimental observations. Consequently, more sophisticated and accurate mean-field schemes have been developed in the literature to accurately describe the mechanical behavior of polycrystalline media. In this area, one can quote the self-consistent scheme [45–47]. This scheme considers each grain as an ellipsoidal inclusion surrounded by an infinite homogeneous effective medium having the average properties of the real polycrystal. Under this scheme, each grain deforms differently from the other grains and intergranular interactions are accurately modeled. Moreover, the equilibrium condition across the grain boundaries is satisfied within the self-consistent approach. This scheme has been coupled in several recent contributions with the FE method [45, 48–50]. The full-field homogenization approaches are generally based on solving the multiscale equations by means of

the FE method, after spatial discretization of the studied polycrystalline aggregate [51–53]. Albeit their undeniable advantages, multiscale approaches present several limitations and issues when they are used to model large-scale metal forming processes by the FE method. In fact, such simulations have the disadvantage of being more computationally burdensome, as they involve a huge amount of CPU time and memory space to store all the microscopic and macroscopic state variables at each time increment. Despite the continuous and growing progress in computer science (robust parallel computations…), these inherent limitations have drastically restricted the use of polycrystalline models in the simulations of sheet metal forming processes.

Clearly, the two modeling approaches (namely, single-scale phenomenological and multiscale approaches) have their own benefits and drawbacks. To combine the strength and the advantages of both approaches, virtual strategies have recently been explored by several authors [54–59]. Within these strategies, multiscale approaches can be used to predict the material mechanical responses for a much larger number of stress or strain loading paths than would be possible by experimental testing. These strategies are enough robust and flexible to accurately identify quite complex phenomena, such as initial and induced plastic anisotropies, distortional hardening, and non-associativity of the flow rules. Combined with appropriate optimization algorithms, the predicted mechanical responses allow fitting the mechanical parameters needed for complex macroscopic phenomenological models. Once the parameters identified, the associated phenomenological models can be used, instead of the multiscale schemes, to robustly simulate metal forming processes. The use of phenomenological models, with the parameters identified on the basis of multiscale computations, leads to an advanced numerical strategy combining the strengths of both modeling approaches: (i) the efficiency of the classical macroscopic phenomenological approaches (as their use involves reduced CPU time), and (ii) the accuracy and physical foundation of multiscale approaches. Consequently, an advanced phenomenological strategy is proposed and implemented in the present work. Within this strategy, the mean-field self-consistent approach is used to model the mechanical behavior of polycrystalline aggregates assumed to be representative of the studied media. The single crystal behavior is modeled by a finite strain rate-independent model, which is more suitable to model the evolution of the mechanical behavior during cold forming processes [60–62]. In this model, the plastic strain is mainly due to the slip along the octahedral crystallographic slip systems (CSSs), and the plastic flow is modeled based on the classical Schmid criterion [63]. Microscopic damage evolution is accounted for in the single crystal modeling by using the framework of continuum damage mechanics approach. The coupling between damage evolution and plastic behavior is based on sound thermodynamics considerations and follows the contributions presented in [22]. Within the present advanced phenomenological strategy, the Barlat yield function [3] is used to describe the initial plastic anisotropy. This yield function is selected considering its reliability and efficiency in the description of

plastic anisotropy of metal alloys. Ductile damage is well-considered in this phenomenological model when the continuum damage mechanics approach is adopted to introduce a scalar damage variable in the constitutive equations. An identification strategy is developed to fit the mechanical parameters corresponding to this model from the self-consistent computations. To model the plastic anisotropy induced by the evolution of crystallographic texture during plastic flow, the identified anisotropy parameters are assumed to evolve during plastic deformation as a function of accumulated plastic strain and damage. The introduction of the anisotropy parameters evolution into the phenomenological model is a pragmatic way to accurately reproduce the mechanical responses predicted by the self-consistent multiscale scheme. Compared to similar approaches developed and used in the literature [54–59], the current modeling presents a new contribution, as the damage evolution is considered in both multiscale and phenomenological approaches. Moreover, robust integration schemes are developed to integrate the different constitutive models, which are implemented as user defined material (UMAT) subroutines into ABAQUS/Standard FE code. The numerical results highlight the reliability of the developed identification strategy and the resulting advanced phenomenological approach.

The outline of the paper is as follows:

- In Section 2, the multiscale and phenomenological constitutive frameworks developed to model the mechanical behavior are shortly presented.
- The identification procedure performed to identify the material parameters corresponding to the advanced phenomenological approach is detailed in Section 3.
- Section 4 presents some numerical results obtained by applying a combined tensile/shear test to highlight the robustness and the reliability of the developed phenomenological strategy.

Conventions, notations and abbreviations

The following conventions and notations are adopted throughout this paper. Note that the assorted notations can be combined, while additional notations will be clarified as needed following related equations:

- Microscale (resp. macroscale) variables are denoted by lowercase (resp. capital) letters.
- Scalar parameters and variables are designated by thin and italic letters or symbols (e.g. a, b).
- Vectors are indicated by boldface letters or symbols with arrow (e.g. $\vec{\mathbf{a}}, \vec{\mathbf{b}}$).
- Second-rank tensors are indicated by boldface letters or symbols (e.g. $\mathbf{a}, \mathbf{b}$).
- Whenever possible, fourth-rank tensors are written as blackboard-bold capital letters to differentiate them from second-order tensors (e.g. $\mathbb{A}, \mathbb{B}$).

- Quantities relating to the grains are systematically indicated by the letter 'gr', while those to the crystallographic slip systems are indicated by letters 'α' or '$.\upsilon.$'.
- $\dot{\bullet}$: time derivative of $\bullet$.
- $\tilde{\bullet}$: the effective counterpart of variable (in the framework of damage mechanics).
- $\bullet^T$: transpose of $\bullet$.
- $\bullet^{-1}$: inverse of $\bullet$.
- $(\bullet)_S$: symmetric part of $\bullet$.
- $(\bullet)_A$: skew-symmetric part of $\bullet$.
- $det(\bullet)$: determinant of $\bullet$.
- $|\bullet|$: absolute value of $\bullet$.
- $\mathrm{sgn}(\bullet)$: sign of $\bullet$ equal to $|\bullet|/\bullet$.
- $\langle\bullet\rangle$: positive part of $\bullet$ or Macaulay brackets equal to $(\bullet+|\bullet|)/2$.
- $\mathrm{e}^{\bullet}$: exponential of $\bullet$.
- $\bullet_{(n)}$: variable $\bullet$ expressed at instant $t_{(n)}$ used in the incremental forms of the different variables (see Section 2.2.3).
- ${}^{n}\bullet$: variable $\bullet$ corresponding to the n^{th} loading in the stress space (see Section 3.1.1).
- $\bullet.\bullet$: simple contraction or contraction on one index (inner product).
- $\bullet:\bullet$: double contraction or contraction on two indices (inner product).
- $\bullet\otimes\bullet$: tensor product (external product).
- $\mathbf{I}_2$: second-rank identity tensor.
- $\mathbb{I}_4$: fourth-rank identity tensor.
- FE: finite element.
- CSS: crystallographic slip system.
- $\mathcal{P}_\phi$: the set of anisotropy parameters defining the anisotropic yield function ϕ.
- $\mathcal{P}_{hd}$: the set of hardening and damage parameters.
- DCCM: damage coupled constitutive modeling.
- DUCM: damage uncoupled constitutive modeling.

- POLY: the mechanical behavior is modeled by the self-consistent polycrystalline approach.
- PHEA: the mechanical behavior is modeled by the phenomenological framework with evolving plastic anisotropy parameters. The evolution of these parameters is fitted on the basis of the polycrystalline simulations.
- PHIA: the mechanical behavior is modeled by the phenomenological framework with constant plastic anisotropy parameters. These parameters are fixed to their initial values identified on the basis of the polycrystalline simulations.
- HYBR: the numerical strategy used to subdivide the specimen in two zones: the weakly loaded zone, where the mechanical behavior is modeled by the PHEA model, and the highly loaded zone, where the POLY model is assigned.

2. Constitutive frameworks

2.1. Multiscale modeling

Compared to classical single crystal models, the present model enables to take into account the effect of microscopic damage on the elastoplastic single crystal behavior. Based on the slip theory, a local micro-damage variable representing the transgranular damage is introduced and fully coupled with the microscopic elastoplastic behavior. The main lines of this damaged constitutive framework will be presented hereafter.

As a starting point of this modeling, the velocity gradient $\mathbf{g}$ is additively partitioned into its symmetric and skew-symmetric parts, denoted as $\dot{\boldsymbol{\varepsilon}}$ and $\mathbf{w}$, respectively. In addition, tensors $\dot{\boldsymbol{\varepsilon}}$ and $\mathbf{w}$ can be split into their elastic and plastic parts:

$$\mathbf{g} = \dot{\boldsymbol{\varepsilon}} + \mathbf{w}, \quad \dot{\boldsymbol{\varepsilon}} = \dot{\boldsymbol{\varepsilon}}^e + \dot{\boldsymbol{\varepsilon}}^p, \quad \mathbf{w} = \mathbf{w}^e + \mathbf{w}^p. \tag{1}$$

Plastic strain is assumed to be mainly due to the slip on crystallographic planes. Hence, tensors $\dot{\boldsymbol{\varepsilon}}^p$ and $\mathbf{w}^p$ are defined as follows [64]:

$$\dot{\boldsymbol{\varepsilon}}^p = \sum_{\alpha=1}^{N_s} \dot{\gamma}^\alpha \left(\mathbf{m}^\alpha\right)_S, \quad \mathbf{w}^p = \sum_{\alpha=1}^{N_s} \dot{\gamma}^\alpha \left(\mathbf{m}^\alpha\right)_A, \tag{2}$$

where:

- $\dot{\gamma}^\alpha$ is the slip rate corresponding to slip system α.
- N_s is the total number of slip systems (equal to 12 for FCC single crystals).

- $\left(\mathbf{m}^{\alpha}\right)_S$ (resp. $\left(\mathbf{m}^{\alpha}\right)_A$) is the symmetric part (resp. skew-symmetric part) of the Schmid orientation tensor $\mathbf{m}^{\alpha}$, which is defined as the tensor product of the unit vector in the slip direction $\vec{\mathbf{b}}^{\alpha}$ and the vector normal to the slip plane $\vec{\mathbf{n}}^{\alpha}$:

$$\forall \alpha = 1,...,N_s: \quad \mathbf{m}^{\alpha} = \vec{\mathbf{b}}^{\alpha} \otimes \vec{\mathbf{n}}^{\alpha}, \tag{3}$$

where the list of vectors $\vec{\mathbf{b}}^{\alpha}$ and $\vec{\mathbf{n}}^{\alpha}$ corresponding to FCC crystallographic structure is provided in Appendix A.

To model the plastic flow in damaged elastoplastic single crystals, the Schmid criterion is extended to take into account the effect of damage evolution on the plastic flow [64]:

$$\forall \alpha = 1,...,N_s: \quad \tilde{f}^{\alpha} = \left|\tilde{\tau}^{\alpha}\right| - \tau_c^{\alpha} \le 0, \quad \operatorname{sgn}\left(\tilde{\dot{\gamma}}^{\alpha}\right) = \operatorname{sgn}\left(\tilde{\tau}^{\alpha}\right), \quad \tilde{\dot{\gamma}}^{\alpha}\,\tilde{f}^{\alpha} = 0, \tag{4}$$

where the effective resolved shear stress $\tilde{\tau}^{\alpha}$ and slip rate $\tilde{\dot{\gamma}}^{\alpha}$ are related to their actual counterparts τ^{α} and $\dot{\gamma}^{\alpha}$ on the basis of the energy equivalence assumption:

$$\forall \alpha = 1,...,N_s: \quad \tilde{\tau}^{\alpha} = \frac{\tau^{\alpha}}{\sqrt{1-d^{\alpha}}}, \quad \tilde{\dot{\gamma}}^{\alpha} = \sqrt{1-d^{\alpha}}\,\dot{\gamma}^{\alpha}, \tag{5}$$

where d^{α} is a scalar damage variable associated with each CSS α, which is defined by the following evolution law equation:

$$\forall\, \alpha = 1,...,N_s: \quad 0 \le d^{\alpha} \le 1, \quad \dot{d}^{\alpha} = \frac{\left|\tilde{\dot{\gamma}}^{\alpha}\right|}{\left(1-d^{\alpha}\right)^{m}} \left(\frac{y^{\alpha} - y_0}{s} \right)^{\theta}. \tag{6}$$

This evolution equation depends on the thermodynamical force y^{α} and on the following material parameters: y_0, s, θ and m.

The actual shear stress τ^{α}, introduced in Eq. (5), is obtained by the twice-contracted tensor product of the microscopic Cauchy stress tensor $\boldsymbol{\sigma}$ by the Schmid tensor $\mathbf{m}^{\alpha}$:

$$\forall \alpha = 1,...,N_s: \quad \tau^{\alpha} = \boldsymbol{\sigma} : \mathbf{m}^{\alpha} = \boldsymbol{\sigma} : \left(\mathbf{m}^{\alpha}\right)_S. \tag{7}$$

Ductile damage is assumed to affect also the elastic properties. In fact, the Cauchy stress tensor $\boldsymbol{\sigma}$ is related to the elastic strain tensor $\boldsymbol{\varepsilon}^e$ (the integral of the elastic strain rate $\dot{\boldsymbol{\varepsilon}}^e$ over the loading history) by the following damaged hypoelastic model [65]:

$$\boldsymbol{\sigma} = \tilde{\mathbf{c}}^e : \boldsymbol{\varepsilon}^e, \tag{8}$$

where the fourth-rank tensor $\tilde{\mathbf{c}}^e$ is the operator of elasticity modulus for the damaged material, which is related to its counterpart for undamaged materiel $\mathbf{c}^e$ by the following classical relationship [66]:

$$\tilde{\mathbf{c}}^e = \left(1 - d_{av}\right)\mathbf{c}^e. \tag{9}$$

The scalar damage variable d_{av} describes the effect of micro-damage on the elastic properties and is expressed as the average of the slip systems damage variables d^α:

$$d_{av} = \frac{1}{N_s}\sum_{\alpha=1}^{N_s} d^\alpha. \tag{10}$$

It should be noted that d_{av} is not a state variable in the thermodynamical sense, but it plays the role of an auxiliary variable.

In the present work, the elasticity of the undamaged material is assumed to be infinitesimal, linear and isotropic. Hence, matrix $\mathbf{c}^e$ only depends on the Young modulus E and the Poisson ratio ν.

The evolution of the critical shear stress is given by the following hardening equation:

$$\forall \alpha = 1,...,N_s: \quad \dot{\tau}_c^\alpha = \sum_{\upsilon=1}^{N_s} h^{\alpha\upsilon}\left|\dot{\gamma}^\upsilon\right|, \tag{11}$$

where $\mathbf{h}$ is the hardening interaction matrix, whose analytical expression is given in details in Appendix A.

A detailed description of the numerical scheme used to integrate the single crystal constitutive equations with damage effect has been provided in [45, 67]. Once the constitutive equations are integrated at the single crystal scale, the self-consistent scheme is then used to obtain the macroscopic response from the microscopic one. The equations defining the self-consistent multiscale scheme are briefly recalled in Appendix B.

2.2. Phenomenological model

2.2.1. Thermodynamic framework

The thermodynamics of irreversible processes and the continuum damage mechanics frameworks are used to formulate the phenomenological model. A state potential is built considering different pairs of state variables describing the different phenomena and using the effective variables concept based on the total energy equivalence assumption to introduce the full coupling of the mechanical behavior and the ductile damage. Thus, three couples of state variables are considered:

- $\left(\mathbf{E}^e, \boldsymbol{\Sigma}\right)$, with $\mathbf{E}^e$ the macroscopic elastic strain tensor,
- $\left(r, R\right)$ representing the isotropic hardening,
- $\left(D, Y\right)$ describing the isotropic damage.

The classical forms of the effective state variables are defined as [20, 22]:

$$\tilde{\boldsymbol{\Sigma}}=\frac{\boldsymbol{\Sigma}}{\sqrt{1-D}},\quad \tilde{\mathbf{E}}^{e}=\sqrt{1-D}\,\mathbf{E}^{e},\quad \tilde{R}=\frac{R}{\sqrt{1-D}},\quad \tilde{r}=\sqrt{1-D}\,r. \tag{12}$$

Note that small elasticity assumption is considered together with large plastic strain. The Helmholtz free energy is chosen as state potential, which is a convex and positive function of the considered strain type state variable:

$$\begin{aligned}\rho\Psi\left(\tilde{\mathbf{E}}^{e},\,\tilde{r}\right)&=\rho\Psi\left(\mathbf{E}^{e},\,r,\,D\right)=\rho\Psi^{e}\left(\mathbf{E}^{e},\,D\right)+\rho\Psi^{h}\left(r,\,D\right)\\&=\frac{1}{2}(1-D)\mathbf{E}^{e}:\mathbb{C}^{e}:\mathbf{E}^{e}+\frac{1}{2}(1-D)Q\,r^{2},\end{aligned} \tag{13}$$

with $\mathbb{C}^{e}$ the fourth-rank elasticity tensor of the undamaged material, and Q the isotropic hardening modulus. From Eq. (13), one can deduce the thermodynamical forces that derive from the state potential:

$$\begin{aligned}&\boldsymbol{\Sigma}=\rho\frac{\partial\Psi}{\partial\mathbf{E}^{\mathbf{e}}}=(1-D)\;\mathbb{C}^{e}:\mathbf{E}^{e},\quad R=(1-D)Qr,\\&Y=-\rho\frac{\partial\Psi}{\partial D}=\frac{1}{2}\mathbf{E}^{e}:\mathbb{C}^{e}:\mathbf{E}^{e}+\frac{1}{2}Qr^{2}=\frac{1}{2}\frac{\boldsymbol{\Sigma}:\mathbb{K}:\boldsymbol{\Sigma}}{(1-D)^{2}}+\frac{1}{2}\frac{R^{2}}{Q(1-D)^{2}}=Y^{e}+Y^{r},\end{aligned} \tag{14}$$

with $\mathbb{K}$ the fourth-rank compliance tensor equal to $\mathbb{C}^{e-1}$. Note that the energy density release rate Y is decomposed in the strain space or in the stress space, due to the full coupling based on total energy equivalence, into an elastic part $Y^{e}=\frac{1}{2}\mathbf{E}^{e}:\mathbb{C}^{e}:\mathbf{E}^{e}=\frac{1}{2}\frac{\boldsymbol{\Sigma}:\mathbb{K}:\boldsymbol{\Sigma}}{(1-D)^{2}}$ and a hardening part $Y^{r}=\frac{1}{2}Qr^{2}=\frac{1}{2}\frac{R^{2}}{Q(1-D)^{2}}$.

To ensure the Clausius–Duhem inequality based on general non-associated plasticity theory, we separately define the yield criterion f and the plastic potential F:

$$f=\phi\left(\tilde{\boldsymbol{\Sigma}}\right)-\left(\Sigma^{Y}+\tilde{R}\right)\leq 0,\quad F=\underline{\phi}\left(\tilde{\boldsymbol{\Sigma}}\right)+R\,H_{1}e^{-H_{2}\bar{E}^{p}}+\frac{1}{(1-D)^{M}}\frac{S}{\Theta+1}\left\langle\frac{Y-Y_{0}}{S}\right\rangle^{\Theta+1}, \tag{15}$$

with:

- Σ^{Y} the initial yield stress,
- ϕ and $\underline{\phi}$ two equivalent stress functions defining the plastic anisotropy of the yield stress and the plastic flow, respectively. Their explicit expressions are provided in Section 2.2.2,
- H_{1} and H_{2} scalar parameters describing the isotropic hardening evolution,
- S, Θ, M and Y_{0} scalar parameters describing the damage evolution,

- $\bar{E}^p$ the accumulated plastic strain measure equal to $\int \sqrt{\dot{\mathbf{E}}^p : \dot{\mathbf{E}}^p}\, dt$.

To accurately reproduce the evolution of plastic anisotropy (resulting from the evolution of the crystallographic texture), the anisotropy parameters involved in the stress state functions ϕ and $\underline{\phi}$ are assumed to evolve with the accumulated plastic strain measure $\bar{E}^p$ and the damage variable D, as will be detailed in Section 3.2.4.

The evolution relations of dissipative phenomena are obtained using the normality rule applied to the plastic potential F :

$$\dot{\mathbf{E}}^p = \dot{\lambda}\frac{\partial F}{\partial \boldsymbol{\Sigma}} = \dot{\lambda}\frac{\partial \underline{\phi}}{\partial \boldsymbol{\Sigma}}\left(\tilde{\boldsymbol{\Sigma}}\right), \tag{16}$$

$$\dot{D} = \dot{\lambda}\frac{\partial F}{\partial Y} = \frac{\dot{\lambda}}{\left(1-D\right)^M}\left\langle \frac{Y - Y_0}{S} \right\rangle^{\Theta}, \tag{17}$$

$$\dot{r} = \dot{\lambda}\frac{\partial F}{\partial R} = \dot{\lambda} H_1 \mathrm{e}^{-H_2 \bar{E}^p}, \tag{18}$$

with $\dot{\lambda}$ the plastic multiplier, implicitly given by the consistency condition or Kuhn–Tucker condition:

$$f \le 0, \quad \dot{\lambda} \ge 0, \quad \dot{\lambda} f = 0, \quad \dot{\lambda}\dot{f} = 0. \tag{19}$$

It shall be noted that the accumulated plastic strain measure $\bar{E}^p$ is different from the equivalent plastic strain $\int \dot{\lambda}\, dt$.

In this model, in addition to the anisotropy parameters defined in ϕ and $\underline{\phi}$, there are eight parameters to be identified (namely, the hardening and damage parameters). These parameters are stored in the set $\mathcal{P}_{hd}$:

$$\mathcal{P}_{hd} = \left\{ Q, \Sigma^Y, H_1, H_2, S, M, \Theta, Y_0 \right\}. \tag{20}$$

2.2.2. Barlat criterion

Due to its reliability, the anisotropic yield criterion introduced in [3] is selected to describe the plastic anisotropy in the phenomenological model. To present the main lines of this criterion, let us introduce the fourth-rank transformation tensor $\mathbb{T}$ relating the effective Cauchy stress tensor $\tilde{\boldsymbol{\Sigma}}$ to a modified effective stress tensor $\tilde{\mathbf{S}}$:

$$\tilde{\mathbf{S}} = \mathbb{T} : \tilde{\boldsymbol{\Sigma}}. \tag{21}$$

The fourth-rank tensor $\mathbb{T}$ allows accurately describing the material plastic anisotropy. Using the Voigt matrix notation, tensor $\mathbb{T}$ can be written in a 6×6 matrix form:

$$\mathbb{T}=\begin{pmatrix} -(T_{12}+T_{13}) & T_{12} & T_{13} & 0 & 0 & 0 \\ T_{12} & -(T_{12}+T_{23}) & T_{23} & 0 & 0 & 0 \\ T_{13} & T_{23} & -(T_{13}+T_{23}) & 0 & 0 & 0 \\ 0 & 0 & 0 & T_{44} & 0 & 0 \\ 0 & 0 & 0 & 0 & T_{55} & 0 \\ 0 & 0 & 0 & 0 & 0 & T_{66} \end{pmatrix}, \tag{22}$$

where T_{ij} are the six anisotropy scalar parameters. Note that some coefficients of the transformation tensor $\mathbb{T}$ verify the relations

$$\forall i=1,..,3: \quad T_{i1}+T_{i2}+T_{i3}=0, \tag{23}$$

arising from invariance of the Barlat criterion upon addition of a mean stress $\tilde{\Sigma}_m=\left(\tilde{\Sigma}_{11}+\tilde{\Sigma}_{22}+\tilde{\Sigma}_{33}\right)$. The anisotropic equivalent stress ϕ, introduced in Eq. (15), can be expressed as function of the eigenvalues $\tilde{S}_1$, $\tilde{S}_2$ and $\tilde{S}_3$ of tensor $\tilde{\mathbf{S}}$ as follows [3]:

$$\phi\left(\tilde{\boldsymbol{\Sigma}}\right)=\left(|\tilde{S}_1-\tilde{S}_2|^A+|\tilde{S}_1-\tilde{S}_3|^A+|\tilde{S}_2-\tilde{S}_3|^A\right)^{1/A}, \tag{24}$$

with exponent A a parameter describing the sharpness of the yield function (typically around 6 for BCC single crystals, and 8 for FCC single crystals). As shown in Eqs. (21)–(24), the yield function ϕ is dependent on seven material parameters, which can be stored in the set $\mathcal{P}_\phi$:

$$\mathcal{P}_\phi=\{T_{12},T_{13},T_{23},T_{44},T_{55},T_{66},A\}. \tag{25}$$

The same form is used for the flow rule anisotropy function $\underline{\phi}$, with eventually a new different set of parameters $\mathcal{P}_{\underline{\phi}}$:

$$\mathcal{P}_{\underline{\phi}}=\{\underline{T}_{12},\underline{T}_{13},\underline{T}_{23},\underline{T}_{44},\underline{T}_{55},\underline{T}_{66},\underline{A}\}. \tag{26}$$

The main lines of the numerical scheme used to integrate the phenomenological constitutive equations are provided in Appendix C.

3. Identification of the advanced model parameters and their evolution laws

This section will focus on the presentation of the identification procedures developed to determine the macroscopic mechanical parameters (and their eventual evolution laws) from the virtual experiments based on the multiscale simulations.

3.1. Generation of the numerical database

3.1.1. Virtual numerical loadings

In order to identify the material parameters (hardening, damage and plastic anisotropy) corresponding to the advanced phenomenological model, we have generated a numerical database by applying a set of 3D numerical tests on a polycrystalline aggregate (assumed to be representative of the studied metallic structure). These numerical tests are linearly applied in the deviatoric stress space, as described by the following conditions:

$$\forall i,j,k,l=1,2,3: \quad \text{stress ratios } \Sigma_{ij}/\Sigma_{kl} \text{ kept constant during the loading and } tr(\boldsymbol{\Sigma})=0. \qquad (27)$$

To cover the whole range of stress modes and then to accurately identify the different mechanical parameters, a large number of loading paths are generally required. This approach, based on the identification of material parameters using virtual experiments, presents several undeniable advantages compared to classical identification based on real experimental tests. In fact, it allows considerably minimizing the identification cost, as testing machines and specimens are not required in this case. Furthermore, this approach enables to reach stress modes not easily reachable due to the limitation of real mechanical experimental tests (such as loadings ${}^{5}\boldsymbol{\Sigma}$ and ${}^{6}\boldsymbol{\Sigma}$ defined in Eq. (29)).

Practically, the evolution laws of parameters T_{12}, T_{13}, T_{23} are identified by applying diagonal macroscopic stress states ${}^{123}\boldsymbol{\Sigma}$ defined by the following form:

$${}^{123}\boldsymbol{\Sigma}(\beta)=\hat{\Sigma}\begin{bmatrix}\cos(\beta) & 0 & 0\\ 0 & \sin(\beta) & 0\\ 0 & 0 & -\cos(\beta)-\sin(\beta)\end{bmatrix}, \qquad (28)$$

where $\hat{\Sigma}$ is the magnitude of the loading and β is the angle defining the stress path direction with respect to the rolling direction. To uniformly sweep the space of deviatoric and diagonal stresses, the angle β is varied between $0°$ and $359°$ with an increment $\Delta\beta=1°$ giving rise then to 360 loadings.

On the other hand, to determine the evolution laws of parameters T_{44}, T_{55}, T_{66}, the following stress loadings are respectively applied:

$${}^{4}\boldsymbol{\Sigma}=\hat{\Sigma}\begin{bmatrix}0&1&0\\1&0&0\\0&0&0\end{bmatrix}, \quad {}^{5}\boldsymbol{\Sigma}=\hat{\Sigma}\begin{bmatrix}0&0&1\\0&0&0\\1&0&0\end{bmatrix}, \quad {}^{6}\boldsymbol{\Sigma}=\hat{\Sigma}\begin{bmatrix}0&0&0\\0&0&1\\0&1&0\end{bmatrix}. \qquad (29)$$

Finally, to better represent the deviatoric stress space and to preserve some balance for the weight of the different parameters T_{ij} in the identification procedure, a set of 100 mixed loadings combining the stress states ${}^{1}\boldsymbol{\Sigma}={}^{123}\boldsymbol{\Sigma}(0)$, ${}^{2}\boldsymbol{\Sigma}={}^{123}\boldsymbol{\Sigma}(90°)$, ${}^{4}\boldsymbol{\Sigma}$, ${}^{5}\boldsymbol{\Sigma}$ or ${}^{6}\boldsymbol{\Sigma}$ are randomly selected from the whole set

of possible combinations and applied. These combined loadings are defined by the following decomposition:

$$\boldsymbol{\Sigma} = k_1 \, {}^{i_1}\boldsymbol{\Sigma} + k_2 \, {}^{i_2}\boldsymbol{\Sigma} + k_3 \, {}^{i_3}\boldsymbol{\Sigma}, \tag{30}$$

with $k_{j=1,\ldots,3} \in \{0, 0.5, 1\}$ and $i_{j=1,\ldots,3} \in \{1, 2, 4, 5, 6\}$. The application of these additional combined loading paths enables to significantly enrich the generated database by integrating more complex loading modes. In total, 463 virtual loading paths are required in the whole to construct the final numerical database. In what follows, those loadings are labeled by an upper index $L_{\boldsymbol{\Sigma}} \in \{1,\ldots,463\}$. For each probing virtual loading $L_{\boldsymbol{\Sigma}}$ and at each n^{th} time increment, the macroscopic plastic strain rate ${}^{L_{\boldsymbol{\Sigma}}}\dot{\mathbf{E}}^{p}_{(n)}$ is deduced from Eq. (B.6):

$${}^{L_{\boldsymbol{\Sigma}}}\dot{\mathbf{E}}^{p}_{(n)} = \sum_{gr=1}^{Ngr} f^{gr} \, {}^{L_{\boldsymbol{\Sigma}}}\dot{\boldsymbol{\varepsilon}}^{p(gr)}_{(n)}. \tag{31}$$

From Eq. (31), one can define the rate of the accumulated plastic strain ${}^{L_{\boldsymbol{\Sigma}}}\dot{\bar{E}}^{p}_{(n)}$ as:

$${}^{L_{\boldsymbol{\Sigma}}}\dot{\bar{E}}^{p}_{(n)} = \sqrt{{}^{L_{\boldsymbol{\Sigma}}}\dot{\mathbf{E}}^{p}_{(n)} : {}^{L_{\boldsymbol{\Sigma}}}\dot{\mathbf{E}}^{p}_{(n)}}. \tag{32}$$

The plastic strain ${}^{L_{\boldsymbol{\Sigma}}}\bar{E}^{p}_{(n)}$ accumulated at the end of the n^{th} time increment can be determined by a time integration of Eq. (32):

$${}^{L_{\boldsymbol{\Sigma}}}\bar{E}^{p}_{(n)} = \int_{0}^{t_{(n)}} {}^{L_{\boldsymbol{\Sigma}}}\dot{\bar{E}}^{p} \, dt. \tag{33}$$

As ${}^{L_{\boldsymbol{\Sigma}}}\dot{\mathbf{E}}^{p}_{(i)}$ is assumed to be constant over the i^{th} time increment, Eq. (33) can be rewritten as follows:

$${}^{L_{\boldsymbol{\Sigma}}}\bar{E}^{p}_{(n)} = \sum_{i=1}^{n} {}^{L_{\boldsymbol{\Sigma}}}\dot{\bar{E}}^{p}_{(i)} \, \Delta t_{(i)} = \sum_{i=1}^{n} \sqrt{{}^{L_{\boldsymbol{\Sigma}}}\dot{\mathbf{E}}^{p}_{(i)} : {}^{L_{\boldsymbol{\Sigma}}}\dot{\mathbf{E}}^{p}_{(i)}} \, \Delta t_{(i)}, \tag{34}$$

where $\Delta t_{(i)}$ is the size of the i^{th} time increment equal to $t_{(i+1)} - t_{(i)}$. The stress state ${}^{L_{\boldsymbol{\Sigma}}}\boldsymbol{\Sigma}_{(n)}$ is stored in the numerical database as the point of the yield locus corresponding to the accumulated plastic strain ${}^{L_{\boldsymbol{\Sigma}}}\bar{E}^{p}_{(n)}$. The points corresponding to the stress states ${}^{L_{\boldsymbol{\Sigma}}}\boldsymbol{\Sigma}_{(n)}$ (for $L_{\boldsymbol{\Sigma}} = 1,\ldots,463$ and $n = 1,\ldots,N$, where N refers to the total number of time increments required to generate the database) define the contour of the yield locus and its evolution, according to the macroscopic accumulated plastic strain obtained by the polycrystalline model for proportional loading paths.

It is worth noting that, as the stress states obtained from the polycrystalline predictions depend in a complex way on the evolution of microstructural variables (such as, slip and damage over the different CSSs of the individual grains and crystallographic texture), which are in turn dependent on the loading

history, the yield loci are strongly dependent on the loading history. Indeed, the evolution of the internal variables at a given stress state is mainly dependent on the loading history (proportional, complex, cyclic…) followed to reach this state. Hence, the proposed phenomenological model is probably limited when it will be used to simulate forming processes with strong and complex loading evolutions (such as crash tests). However, for classical forming processes (such as deep drawing or rolling), one expects that local loading paths do not exhibit strong deviations from proportional loadings, so that the proposed numerical strategy remains relevant in this case.

3.1.2. Polycrystal material parameters

The multiscale simulations required to generate the numerical database are performed using a FCC polycrystalline aggregate made of five hundred grains. The initial crystallographic texture, typical for cold-rolled polycrystals, corresponding to this aggregate is plotted in the form of (100) and inverse pole figures in Fig. 1.

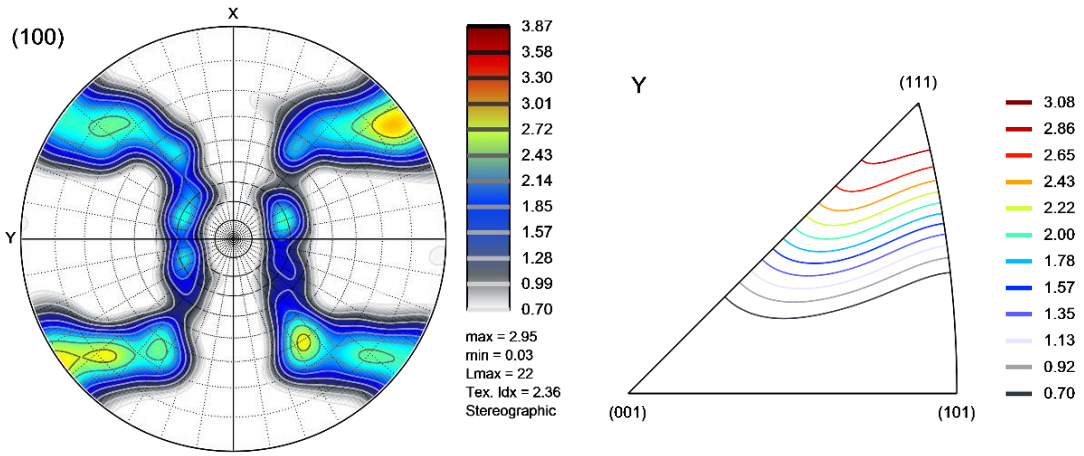

(a) (b)

Fig. 1. Initial crystallographic texture for cold-rolled polycrystal generated by the ATEX software [68]: (a) (100) pole figure; (b) inverse pole figure with respect to the Y direction.

The microscopic material parameters used to apply the virtual loadings are provided in

Table 1. These material parameters correspond to the Waspaloy alloy and are identified in [65] based on several experimental tests.

Table 1. Microscopic material parameters [65].

Hardening parameters (see Appendix A)								
τ_0 (MPa)	h_0 (MPa / s)	b	a_1	a_2	a_3	a_4	a_5	a_6
320	356	14.9	1.0	0.86	1.01	1.14	1.3	3.13

Elasticity parameters		**Damage parameters (see Eq. (6))**			
E (GPa)	v	s (MPa)	θ	m	y_0 (MPa)
200	0.3	30	1	0.85	0

3.2. Identification procedure

Once the numerical database is built by the method detailed in Section 3.1.1, the optimal parameters of the phenomenological model should be identified, in such a way that the phenomenological predictions allow closely reproducing the polycrystalline macroscopic mechanical responses for linear stress paths. This objective is to be reached assuming that the components of the transformation tensor $\mathbb{T}$ evolve as functions of the accumulated plastic strain $\bar{E}^p$ and ductile damage variable D. This evolution is integrated in the phenomenological modeling to accurately follow the microstructural evolutions exhibited by the polycrystalline model, thus leading to the evolution of the macroscopic plastic anisotropy. The resulting model, taking into account the evolution of the anisotropy parameters, can be viewed as advanced phenomenological modeling, since it allows combining the strengths of both models: the self-consistent modeling to accurately reproduce the evolution of plastic anisotropy, and the initial phenomenological modeling to efficiently predict the mechanical behavior. To further investigate the effect of damage evolution on the identified results, the cases with and without full coupling with damage will be separately considered. These cases will be briefly denoted in what follows DCCM and DUCM, respectively.

3.2.1. Identification steps

Due to the large number of parameters involved in the phenomenological model, it is extremely complicated to simultaneously determine the optimal set of these parameters with the suitable evolution laws. To overcome this issue, a sequential identification strategy including the following

successive steps is performed:

1. Using the mechanical response obtained by the application of the loading ${}^{1}\boldsymbol{\Sigma} = {}^{123}\boldsymbol{\Sigma}(0)$ (see Eq. (28) to recall the explicit expression of this loading), determine the hardening and damage parameters belonging to set $\mathcal{P}_{hd}$ by applying the identification procedure detailed in Section 3.2.2.
2. For each accumulated plastic strain level $\bar{E}^{p}_{(n)}$ (for $n = 1, \ldots, N$), compute the set of macroscopic stress states ${}^{L_\Sigma}\boldsymbol{\Sigma}_{(n)}$ (with $L_\Sigma = 1, \ldots, 463$) and generate on the basis of this set the numerical yield locus. Thereafter, deduce the damage variables ${}^{L_\Sigma}D_{(n)}$ corresponding to the different stress states ${}^{L_\Sigma}\boldsymbol{\Sigma}_{(n)}$. Finally, identify the optimal plastic anisotropy parameters. To simplify the running of this identification strategy, associated flow rule is assumed in this step. Hence, only the sets $\mathcal{P}_{\phi}\left(\bar{E}^{p}_{(n)}, {}^{L_\Sigma}D_{(n)}\right)$ corresponding to the anisotropic function ϕ should be identified, while sets $\mathcal{P}_{\underline{\phi}}\left(\bar{E}^{p}_{(n)}, {}^{L_\Sigma}D_{(n)}\right)$ are identically equal to $\mathcal{P}_{\phi}\left(\bar{E}^{p}_{(n)}, {}^{L_\Sigma}D_{(n)}\right)$. Further details about the technical aspects related to this step will be provided in Section 3.2.3. The identification of the plastic anisotropy parameters will be improved in Step 4 by considering the non-associativity of the plastic flow.
3. Using the numerical database generated in Step 2, determine the evolution laws of the anisotropy parameters belonging to set $\mathcal{P}_{\phi}$ on the basis of the methodology detailed in Section 3.2.4.
4. Improve the identification of the plastic anisotropy parameters by considering the non-associativity of the plastic flow. This step will be detailed in Section 3.2.5.

The developed identification methodology is schematically illustrated by the flowchart of Fig. 2. For the sake of readability of this flowchart, only the first three steps of this identification strategy are presented in this figure. It should be recalled that the decomposition of the above-defined steps, instead of simultaneous identification of all parameters, allows easily checking, at each step of the identification procedure, the reliability and physical consistency of the obtained parameters. In particular, this enables to determine the functions describing the evolution of plastic anisotropy parameters (Section 3.2.3), so that to comply with the numerical evolution obtained in Step 2.

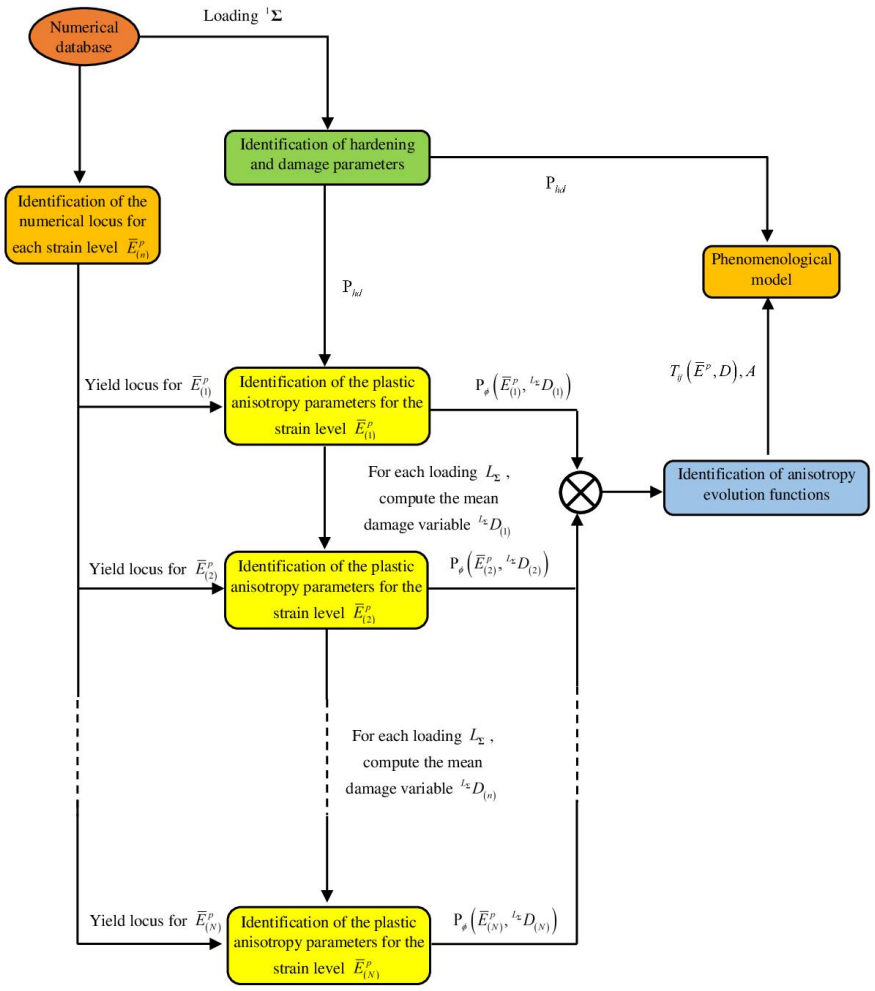

Fig. 2. Flowchart of the identification procedure (only the first three steps are illustrated).

3.2.2. Identification of the hardening and damage parameters

The identification of the hardening and damage parameters is performed using the evolution of the stress state ${}^{1}\boldsymbol{\Sigma}$ corresponding to the first loading path. This stress state, explicitly defined in Section 3.1.1, can be expressed as a function of the von Mises equivalent stress ${}^{1}\Sigma_{vMeq}$:

$$ {}^{1}\boldsymbol{\Sigma} = \frac{{}^{1}\Sigma_{vMeq}}{\sqrt{3}} \begin{bmatrix} 1 & 0 & 0 \\ 0 & 0 & 0 \\ 0 & 0 & -1 \end{bmatrix}. \tag{35} $$

In order to maintain the consistency of the constitutive modeling and to respect the description of the plastic anisotropy by the Barlat criterion, the following equality should be fulfilled at the end of each time increment n:

$$ \forall n = 1,\ldots,N: \quad \phi\left({}^{1}\boldsymbol{\Sigma}_{(n)}\right) = {}^{1}\Sigma_{vMeq(n)}. \tag{36} $$

For each time increment, the previous equation leads to a nonlinear relation between the six components of the transformation matrix $\mathbb{T}$ (namely, T_{12}, T_{13}, T_{23}, T_{44}, T_{55}, and T_{66}). Then, one component of matrix $\mathbb{T}$ can be expressed as function of the five other components to ensure the satisfaction of Eq. (36). From the incremental form of Eq. (C.8), one can deduce that:

$$f_{(n)} = \phi\left({}^{1}\tilde{\boldsymbol{\Sigma}}_{(n)}\right) - \left(\Sigma^{Y} + {}^{1}\tilde{R}_{(n)}\right) = \frac{{}^{1}\Sigma_{vMeq(n)}}{\sqrt{1-{}^{1}D_{(n)}}} - \left(\Sigma^{Y} + \frac{{}^{1}R_{(n)}}{\sqrt{1-{}^{1}D_{(n)}}}\right) = 0, \tag{37}$$

where ${}^{1}R_{(n)}$ and ${}^{1}D_{(n)}$ are obtained from the incremental forms described by Eqs. $(C.6)_1$ and $(C.7)_1$, respectively. Scalars ${}^{1}R_{(n)}$ and ${}^{1}D_{(n)}$ are mainly dependent on the damage and hardening parameters. Then, one can define the quadratic error function to minimize, with respect to the components of set $\mathcal{P}_{hd}$, by the least square method:

$$\mathrm{Err}_{hd}\left(\mathcal{P}_{hd}\right) = \left(\sum_{n=1}^{N}\left(\frac{{}^{1}\tilde{\Sigma}_{vMeq(n)} - \left(\Sigma^{Y} + {}^{1}\tilde{R}_{(n)}\left(\mathcal{P}_{hd}\right)\right)}{{}^{1}\tilde{\Sigma}_{vMeq(n)}}\right)^{2}\right)^{1/2}. \tag{38}$$

Optimal parameters are obtained using the Levenberg–Marquardt minimization algorithm implemented in MATLAB through the *lsqcurvefit* function. This algorithm is based on the interior-reflective Newton method described in [69]. Comparisons between the polycrystalline (POLY) and phenomenological (PHEN) predictions, in terms of the evolution of the equivalent stress ${}^{1}\Sigma_{vMeq}$ as a function of the accumulated plastic strain $\bar{E}^{p}$, are displayed in Fig. 3. The results of this figure reveal the perfect agreement between the polycrystalline simulations and the phenomenological predictions, thus highlighting the accuracy of the fitted parameters. The complete sets of hardening and damage parameters, identified on the basis of polycrystalline simulations, are summarized in Table 2 and Table 3.

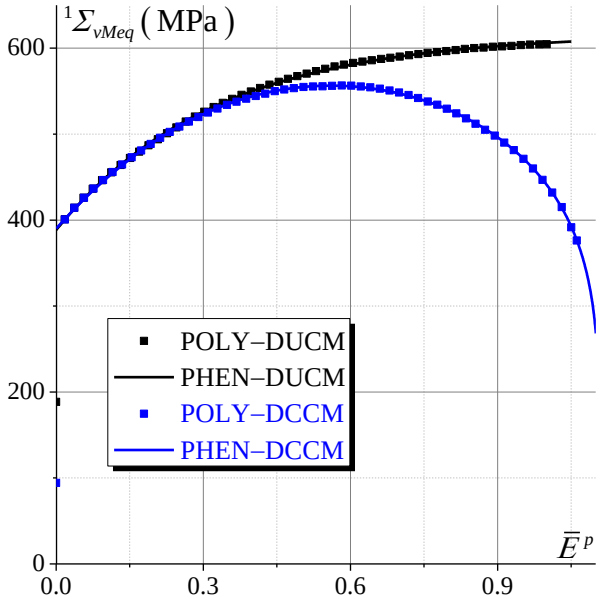

Fig. 3. Hardening and damage identification results: evolution of the von Mises equivalent stress $^1\Sigma_{vMeq}$ as a function of the accumulated plastic strain $\bar{E}^p$.

Table 2. Hardening parameters belonging to set $\mathcal{P}_{hd}$, identified on the basis of polycrystalline simulations without considering microscopic damage (DUCM).

Hardening			
Σ^Y (MPa)	Q (MPa)	H_1	H_2
388.3	6.851	102.5	3.075

Table 3. Hardening and damage parameters belonging to set $\mathcal{P}_{hd}$, identified on the basis of polycrystalline simulations considering microscopic damage (DCCM).

Hardening				**Damage**			
Σ^Y (MPa)	Q (MPa)	H_1	H_2	S (MPa)	Θ	M	Y_0 (MPa)
390.0	9.19	69.87	2.316	7193.	1.02	2.65	0.

To further analyze the predictions obtained by the polycrystalline model and those obtained by the phenomenological one when loading is applied, the evolution of the phenomenological damage variable ^1D and the polycrystalline damage variable $^1D^{POLY}$ are plotted as functions of the accumulated plastic strain $\bar{E}^p$ in Fig. 4. The damage variable ^1D is obtained by the incremental Eq. (C.6)$_1$, while the evolution law of variable $^1D^{POLY}$ is given by the following two-level averaging expression:

$$ {}^{1}\dot{D}^{POLY} = \sum_{gr=1}^{Ngr} f^{gr} \frac{1}{\mathrm{card}\left({}^{1}\mathcal{A}^{gr}\right)} \sum_{\alpha=1}^{Ns} {}^{1}\dot{d}^{\alpha(gr)}, \tag{39} $$

where $\mathrm{card}\left({}^{1}\mathcal{A}^{gr}\right)$ is the total number of active slip systems activated during the loading history in grain gr.

It should be noted that D^{POLY} is not a classical state variable in the thermodynamical sense, but an auxiliary variable. Indeed, this variable is not derived from a macroscopic thermodynamical force. As clearly shown by Eq. (39), this variable characterizes the mean damage over all the microscopic constituents of the polycrystalline aggregate (individual grains and slip systems). This polycrystalline variable is obviously equal to unity when all the grains of the aggregate are completely damaged (i.e., when the microscopic damage variable $d^{\alpha(gr)}$ reaches the value of unity for at least one slip system α in each individual grain gr). On the other hand, the phenomenological damage variable D describes the macroscopic stress softening and the degradation of the macroscopic mechanical properties due to the micro-cracks and micro-cavities that develop within the material as the applied loading increases. This latter variable characterizes the apparent damage at the macroscopic level (softening of the macroscopic stress), regardless of what happens at the microscopic scale. This variable reaches unity when the macroscopic stress vanishes. By contrast to D^{POLY}, variable D is a consistent thermodynamical variable as it derives from a macroscopic thermodynamical force as shown in Eq. (17).

Trends observed on Fig. 4 reveal that the evolutions of the two damage variables (namely, ${}^{1}D^{POLY}$ and ${}^{1}D$) are quite different. Indeed, when damage increases in the polycrystalline aggregate, the deformation tends to localize in most damaged grains, while other grains remain undamaged. As a result, there is significant softening of the macroscopic stress inducing an important increase of the phenomenological damage variable ${}^{1}D$. On the other hand, at macroscopic failure (characterized by ${}^{1}D=1$), several grains in the polycrystalline aggregate remain undamaged or slightly damaged. Then, at this moment, variable ${}^{1}D^{POLY}$ remains low (significantly smaller than unity). The difference observed in the evolution of the two damage measures (namely ${}^{1}D$ and ${}^{1}D^{POLY}$) implies that D^{POLY} cannot be considered as relevant macroscopic damage variable, as classically used in the continuum damage mechanics framework. Hence, the evolution of variable D^{POLY} cannot be used to identify the macroscopic damage parameters.

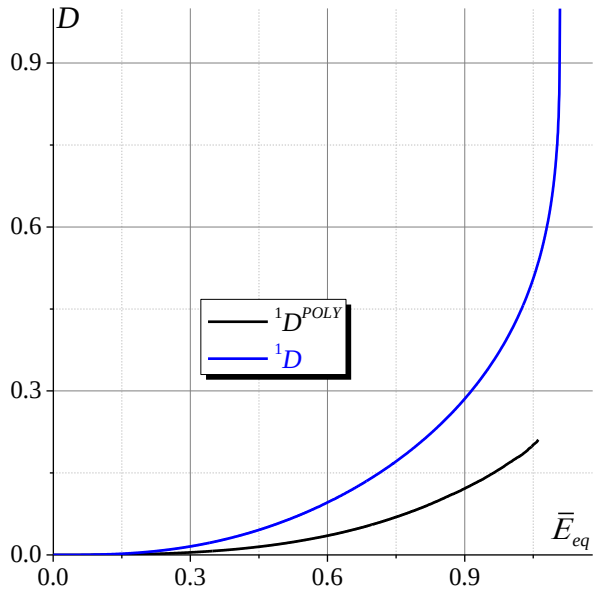

Fig. 4. Evolution of phenomenological and polycrystalline damage variables ${}^{1}D$ and ${}^{1}D^{POLY}$ as functions of the accumulated plastic strain $\bar{E}^{p}$ predicted by applying loading ${}^{1}\boldsymbol{\Sigma}$.

It should be noted that the choice of the macroscopic loading in the identification procedure (${}^{1}\boldsymbol{\Sigma}$ in this case) has an impact on the values of the identified hardening and damage parameters. Indeed, different choices for the applied loading lead to different values of parameters constituting $\mathcal{P}_{hd}$. Nevertheless, the comparisons between the phenomenological mechanical responses obtained with the different sets $\mathcal{P}_{hd}$ optimized on the basis of different loadings ${}^{L_\Sigma}\boldsymbol{\Sigma}$ show very small discrepancies. In fact, the successive optimization procedures described in Step 2 and Step 3 of Section 3.2.1 tend to reduce the differences induced by the choice of the applied loading made in Step 1.

3.2.3. Identification of the associated plastic anisotropy parameters

As explained in Section 3.2.1, the plastic flow rule is firstly assumed to be associated (i.e., $\mathcal{P}_{\phi} = \mathcal{P}_{\underline{\phi}}$), and the corresponding anisotropy parameters are identified in the current section. This identification is incrementally performed, where the set $\mathcal{P}_{\phi(n)}$ corresponding to the accumulated plastic strain level $\bar{E}^{p}_{(n)}$ is used to identify the set $\mathcal{P}_{\phi(n+1)}$ corresponding to the strain level $\bar{E}^{p}_{(n+1)}$. The developed identification procedure is defined by the following steps:

- Knowing the mechanical variables at the end of the n^{th} increment (namely, ${}^{L_\Sigma}\boldsymbol{\Sigma}_{(n)}$, $\bar{E}^{p}_{(n)}$, ${}^{L_\Sigma}D_{(n)}$, and ${}^{L_\Sigma}r_{(n)}$) and the set $\mathcal{P}_{\phi(n)}$, determine ${}^{L_\Sigma}D_{(n+1)}$ and ${}^{L_\Sigma}r_{(n+1)}$ using the explicit incremental form of Eqs. (17) and (18):

$$ {}^{L_\Sigma}D_{(n+1)} = {}^{L_\Sigma}D_{(n)} + \frac{{}^{L_\Sigma}\Delta\mathcal{M}}{\left(1-{}^{L_\Sigma}D_{(n)}\right)^{M}}\left\langle \frac{{}^{L_\Sigma}Y_{(n)}-Y_0}{S}\right\rangle^{\Theta} \quad , \quad {}^{L_\Sigma}r_{(n+1)} = {}^{L_\Sigma}r_{(n)} + {}^{L_\Sigma}\Delta\mathcal{M}\,H\left(\bar{E}^{p}_{(n)}\right). \tag{40} $$

- Use the mechanical variables ${}^{L_\Sigma}\boldsymbol{\Sigma}_{(n+1)}$ and $\bar{E}^{p}_{(n+1)}$ stored in the database in addition to the fields ${}^{L_\Sigma}D_{(n+1)}$ and ${}^{L_\Sigma}r_{(n+1)}$ computed by Eq. (40) to identify the parameters belonging to set $\mathcal{P}_{\phi(n+1)}$ (namely, the components of the transformation matrix $\mathbb{T}_{(n+1)}$ and exponent $A_{(n+1)}$) by minimizing the quadratic error function $\mathrm{Err}_{\phi(n+1)}$ defined as follows:

$$ \mathrm{Err}_{\phi}\left(\mathcal{P}_{\phi(n+1)}\right) = \left(\sum_{L_\Sigma=1}^{463} \left(\frac{\phi\left({}^{L_\Sigma}\tilde{\boldsymbol{\Sigma}}_{(n+1)}, \mathcal{P}_{\phi(n+1)}\right) - \left(\Sigma^{Y} + {}^{L_\Sigma}\tilde{R}_{(n+1)}\right)}{\phi\left({}^{L_\Sigma}\tilde{\boldsymbol{\Sigma}}_{(n+1)}, \mathcal{P}_{\phi(n+1)}\right)} \right)^{2} \right)^{1/2} . \tag{41} $$

The MATLAB function *lsqcurvefit*, based on the Levenberg–Marquardt minimization algorithm, is again used to minimize the error function (41) and then to fit the parameters belonging to set $\mathcal{P}_{\phi(n+1)}$.

To evaluate the accuracy of the identification of anisotropy parameters when the DUCM is used, the yield loci obtained by the polycrystalline simulations are compared with those predicted by the phenomenological model for $\bar{E}^{p}=0.01$ and $\bar{E}^{p}=0.6$ in Fig. 5a and Fig. 5b, respectively. To plot the phenomenological yield loci, two sets of plastic anisotropy parameters have been used: the initial parameters identified at the beginning of the plastic deformation (PHIA) and the updated parameters (PHEA) identified at $\bar{E}^{p}=0.01$ for Fig. 5a and $\bar{E}^{p}=0.6$ for Fig. 5b. In view of the results of Fig. 5, some conclusions can be drawn:

- The reliability and efficiency of the identification procedure is clearly confirmed by the good agreement between the polycrystalline yield surface and the phenomenological one predicted using the evolving anisotropy parameters (parameters identified at the corresponding accumulated plastic strain level).
- The yield loci of Fig. 5b highlight the interest of the incremental identification of the plastic anisotropy parameters to accurately reproduce the polycrystalline yield locus. In fact, the polycrystalline yield surface perfectly agrees with the phenomenological yield surface predicted with the evolving anisotropy parameters; is the latter being quite different from its counterpart determined by the initial anisotropy parameters.

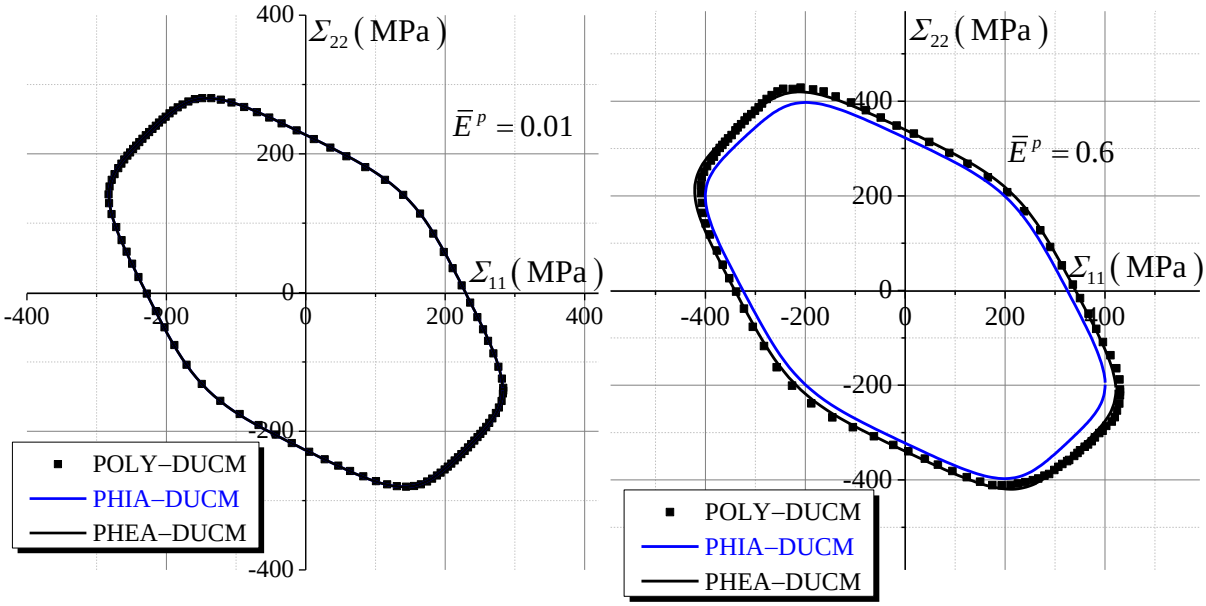

(a) (b)

Fig. 5. Comparison between polycrystalline and phenomenological yield loci plotted at: (a) $\bar{E}^p = 0.01$, and (b) $\bar{E}^p = 0.6$ (predictions obtained by DUCM).

For the DCCM, the evolution of the yield loci is quite similar to the ones presented in Fig. 5 until the stage when the damage becomes significant. In fact, the DCCM is unable to accurately reproduce the evolution of the polycrystalline yield locus in the final damage stage. The yield loci predicted at $\bar{E}^p = 1.05$ by considering the damage evolution in both models (DCCM) are plotted in Fig. 6a. Comparison with the uncoupled models at the same stage of deformation is provided in Fig. 6b to highlight the influence of the damage on the yield loci. As shown in Fig. 6a, the damage effect becomes important leading to a decrease of the stress level due to the softening phenomenon and to an important interaction between damage and crystallographic texture evolutions. Furthermore, the polycrystalline simulations lead to a six-point star-shaped yield locus, revealing a remarkable effect of anisotropic damage evolution observed at the macroscopic level [25]. On the other hand, the phenomenological yield loci keep their classic convex shape. The nonconvex star-shaped yield locus obtained with the polycrystalline model is due to the fact that this surface does not represent a yield surface in an exact manner, but rather an iso-accumulated plastic strain contour (defined at $\bar{E}^p = cte$). Noting that for a given loading direction, the polycrystalline model can induce more or less plastic strain and damage, depending on the orientation of the loading with respect to the texture evolution of the material. The peaks of the star-loci represent the stress directions of low slip systems activation; however, the hollows represent the stress directions of high slip systems activation. The difference observed between polycrystalline yield locus and its phenomenological counterparts highlights an interesting effect of anisotropic damage evolution, which is also not easy to investigate with real

experimental tests. The proposed methodology can offer as well an interesting possibility to identify and determine more sophisticated phenomenological models, on the basis of polycrystalline predictions, including for example anisotropic damage [25].

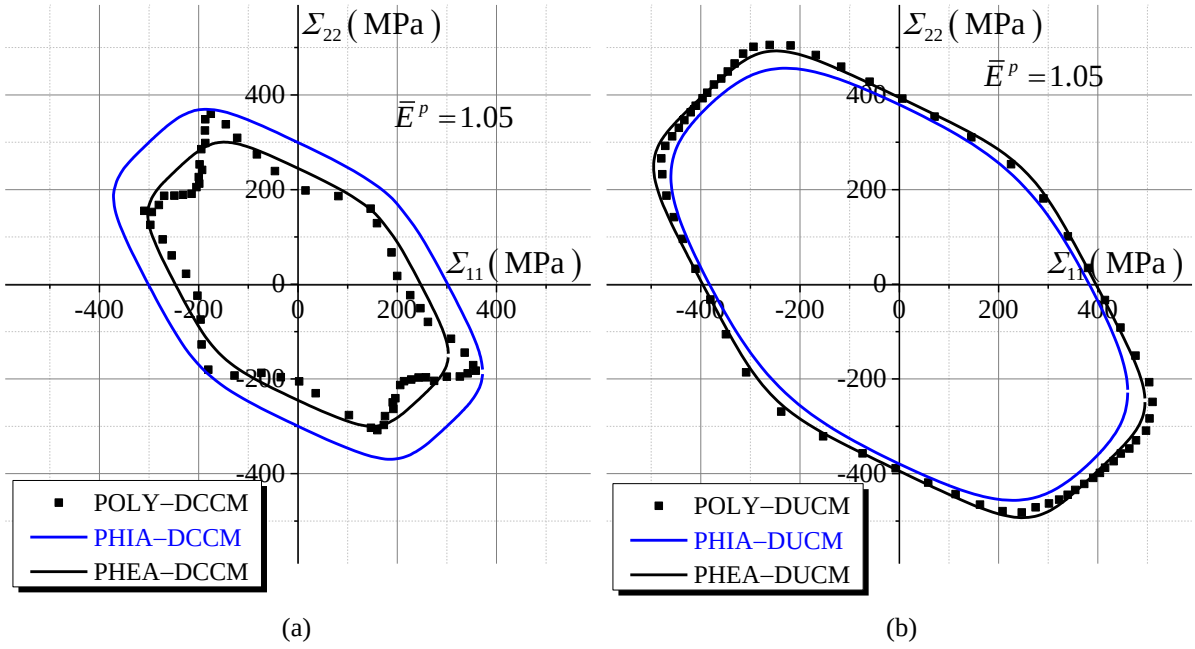

Fig. 6. Comparison between polycrystalline and phenomenological yield loci plotted at $\bar{E}^p = 1.05$: (a) Predictions obtained by DCCM , and (b) Predictions obtained by DUCM.

3.2.4. Identification of the functions describing the evolving plastic anisotropy (associated flow rule)

For each loading level, the values of anisotropy parameters T_{ij} and exponent a belonging to set $\mathcal{P}_\phi$ have been determined using the identification procedure detailed in Section 3.2.3. A first analysis of the results given by this identification procedure reveals that exponent a slowly evolves during the loading history and its value is around 9. Then, this value is used in the remainder of the paper. The numerical database generated in Section 3.2.3 is used in the current section to fit analytical evolution laws for parameters T_{ij}. Explicit expressions of functions T_{ij} will be provided in the following developments, where the cases without and with consideration of damage evolution will be separately studied (as the trends significantly depend on the consideration or not of damage evolution).

- Identification using DUCM

The evolution of the components T_{ij} of the transformation matrix as functions of the accumulated plastic strain $\bar{E}^p$ has been firstly analyzed. It turns out from this analysis that the evolution of these components shall follow two main stages:

- *Transient hardening stage*, where plastic anisotropy evolves rapidly with respect to the accumulated plastic strain. This fast evolution is mainly due to the rapid changes in the activity of slip systems observed at the beginning of the plastic loading in the individual grains.
- *Permanent plasticity stage*, where the hardening is almost saturated. This stage is characterized by a slow evolution of plastic anisotropy.

On the basis of this analysis, the evolution law

$$T_{ij}\left(\bar{E}^p\right)=\left(A_{ij}^1+A_{ij}^2\,e^{-k_{ij}^1\bar{E}^p}\right)g_{ij}^1\left(\bar{E}^p\right)g_{ij}^2\left(\bar{E}^p\right), \tag{42}$$

has been selected, as it matches quite well the sampling points for all the components T_{ij}. This evolution law, developed in the same spirit as the laws used in [70], depends on the fitting parameters A_{ij}^1, A_{ij}^2, k_{ij}^1 and functions g_{ij}^1 and g_{ij}^2, which evolve according to the following evolution rules:

$$g_{ij}^1\left(\bar{E}^p\right)=1+g_{ij}^{11}\,e^{-g_{ij}^{12}\left(\bar{E}^p-g_{ij}^{13}\right)^2},\quad g_{ij}^2\left(\bar{E}^p\right)=1+g_{ij}^{21}\,e^{-g_{ij}^{22}\left(\bar{E}^p-g_{ij}^{23}\right)^2}\quad\text{with}\quad g_{ij}^{12}>0\quad\text{and}\quad g_{ij}^{22}>0, \tag{43}$$

where g_{ij}^{11}, g_{ij}^{12}, g_{ij}^{13}, g_{ij}^{21}, g_{ij}^{22}, and g_{ij}^{23} are fitting parameters, while term $A_{ij}^1+A_{ij}^2\,e^{-k_{ij}^1\bar{E}^p}$ describes the global evolution of the components T_{ij} with $\bar{E}^p$. One has added the functions g_{ij}^1 and g_{ij}^2 to describe small bumps in the evolution of $T_{ij}\left(\bar{E}^p\right)$ (see Fig. 7). Indeed, g_{ij}^1 (resp. g_{ij}^2) induces a small modification in the evolution of $T_{ij}\left(\bar{E}^p\right)$ for $\bar{E}^p$ close to g_{ij}^{13} (resp. close to g_{ij}^{23}). The different fitting parameters are stored in the set $\mathcal{P}_{ij}^{\Gamma}$:

$$\mathcal{P}_{ij}^{\Gamma}=\left\{A_{ij}^1,A_{ij}^2,k_{ij}^1,g_{ij}^{11},g_{ij}^{12},g_{ij}^{13},g_{ij}^{21},g_{ij}^{22},g_{ij}^{23}\right\}. \tag{44}$$

The numerical values of the different components of set $\mathcal{P}_{ij}^{\Gamma}$ are identified by minimizing the following function:

$$\mathrm{Err}\left(\mathcal{P}_{ij}^{\Gamma}\right)=\left(\sum_{n=1}^{N}\left(\frac{T_{ij}^{DISC}\left(\bar{E}_{(n)}^p\right)-T_{ij}^{PHEA}\left(\bar{E}_{(n)}^p,\mathcal{P}_{ij}^{\Gamma}\right)}{T_{ij}^{DISC}\left(\bar{E}_{(n)}^p\right)}\right)^2\right)^{1/2}, \tag{45}$$

where T_{ij}^{DISC} are the discrete values of T_{ij} determined from the database constructed on the basis of the results of Section 3.2.3, and T_{ij}^{PHEA} are the values of T_{ij} determined by the evolution law of Eq. (42). The accuracy of the identification procedure is clearly shown in Fig. 7, where the evolutions of the discrete values T_{ij}^{DISC} are favorably compared with the evolutions of T_{ij}^{PHEA}.

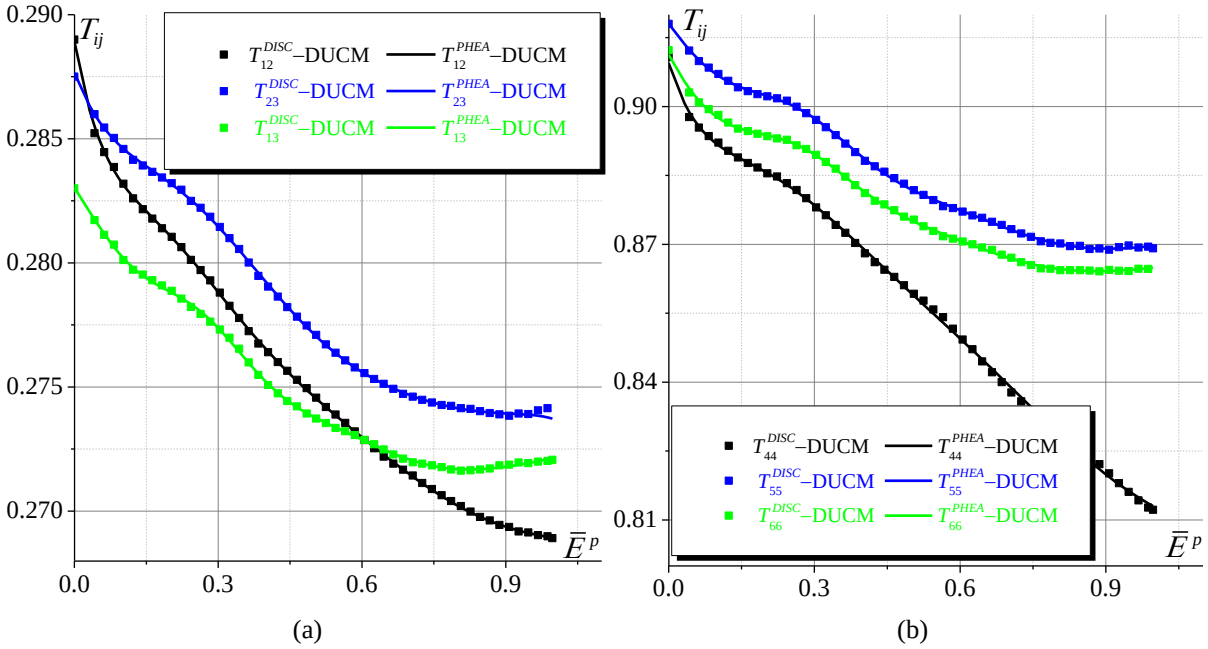

Fig. 7. Evolution of the anisotropy parameters (identification with DUCM): (a) Components T_{12}, T_{23}, and T_{13}, and (b) Components T_{44}, T_{55}, and T_{66}.

The values of the different fitting parameters, optimized with DUCM, are provided in Table 4.

Table 4. Identification of the fitting parameters (DUCM).

	A^1	A^2	k^1	g^{11}	g^{12}	g^{13}	g^{21}	g^{22}	g^{23}
T_{12}	0.269	0.0099	15.4	2310	2.41	2.27	2960	9.57	0.902
T_{13}	0.272	0.0547	6.63	-0.763	12.5	0.0236	0.0236	67.6	0.827
T_{23}	0.274	0.0081	12.2	-1.86	19.3	-165	-165	9.03	0.844
T_{44}	0.783	1.51	3.52	-0.978	0.938	-0.059	-0.059	1.3	-2.22
T_{55}	0.904	0.0213	6.58	-71100	2.36	2.32	2.32	48	0.2
T_{66}	0.864	0.0144	12.4	-0.169	58.8	0.11	0.11	5.64	1.14

- Identification using DCCM

After careful analysis, we have observed that the anisotropy parameters identified by DCCM evolve in three main stages: transient hardening and permanent plasticity stages (very similar to those observed with DUCM), followed by a final damaging stage. In this last stage, damage increase hastens up to failure, inducing again rapid plastic anisotropy evolution. On the basis of these observations, we have tried several functions to describe the evolutions of T_{ij} as functions of $\bar{E}^p$ and D, and we have selected the following law, which seems to be the most appropriate:

$$T_{ij}\left(\bar{E}^p, D\right) = A_{ij}^1 + A_{ij}^2 e^{-k_{ij}^1 \bar{E}^p} + A_{ij}^3 \bar{E}^p + A_{ij}^4 \left(\bar{E}^p\right)^2 + \frac{A_{ij}^5}{1-D}. \tag{46}$$

In the evolution law (46), parameters A_{ij}^2, A_{ij}^3, A_{ij}^4 and k_{ij}^1 (resp. parameter A_{ij}^5) reflect the influence of the plastic deformation (resp. damage) on the evolution of the anisotropy parameter T_{ij}. The different fitting parameters are stored in the set $\mathcal{P}_{ij}^r$:

$$\mathcal{P}_{ij}^r = \left\{ A_{ij}^1, A_{ij}^2, A_{ij}^3, A_{ij}^4, A_{ij}^5, k_{ij}^1 \right\}. \tag{47}$$

The numerical values of the different components of $\mathcal{P}_{ij}^r$ are identified by minimizing the following function:

$$\mathrm{Err}\left(\mathcal{P}_{ij}^r\right) = \left(\sum_{n=1}^{N} \left(\frac{T_{ij}^{DISC}\left(\bar{E}_{(n)}^p, D_{(n)}^{MEAN}\right) - T_{ij}^{PHEA}\left(\bar{E}_{(n)}^p, D_{(n)}^{MEAN}, \mathcal{P}_{ij}^r\right)}{T_{ij}^{DISC}\left(\bar{E}_{(n)}^p, D_{(n)}^{MEAN}\right)} \right)^2 \right)^{1/2}, \tag{48}$$

with $D_{(n)}^{MEAN}$ the mean value of ${}^{L_\Sigma}D_{(n)}$ over all the loading paths L_Σ at the deformation level $\bar{E}_{(n)}^p$:

$$D_{(n)}^{MEAN} = \frac{1}{463} \sum_{L_\Sigma=1}^{463} {}^{L_\Sigma}D_{(n)}. \tag{49}$$

It should be noted that the optimization of the parameters belonging to set $\mathcal{P}_{ij}^r$, considering the fluctuations of the phenomenological damage variable D for the different loadings, would better reflect the complexity of the polycrystalline mechanical behavior. In this case, the error function should read:

$$\mathrm{Err}\left(\mathcal{P}_{ij}^r\right) = \left(\sum_{n=1}^{N} \sum_{L_\Sigma=1}^{463} \left(\frac{T_{ij}^{DISC}\left(\bar{E}_{(n)}^p, {}^{L_\Sigma}D_{(n)}\right) - T_{ij}^{PHEA}\left(\bar{E}_{(n)}^p, {}^{L_\Sigma}D_{(n)}, \mathcal{P}_{ij}^r\right)}{T_{ij}^{DISC}\left(\bar{E}_{(n)}^p, {}^{L_\Sigma}D_{(n)}\right)} \right)^2 \right)^{1/2}. \tag{50}$$

However, the numerical predictions have shown very few fluctuations of ${}^{L_\Sigma}D_{(n)}$ for the different loading paths. Indeed, all ${}^{L_\Sigma}D_{(n)}$ values remain very close to $D_{(n)}^{MEAN}$. Then, the use of the error function (50) does not provide a significant improvement of the identification strategy. Hence, for the sake of simplicity and in order to reduce the computational effort required by the application of the identification procedures, one chooses to use the error function (49).

By comparing the curves of Fig. 7 and Fig. 8, it clearly appears that the anisotropy parameters evolutions are strongly affected by the damage occurrence. This justifies the proposed law of Eq. (46), which can fit the evolution of parameters T_{ij} with convincing accuracy.

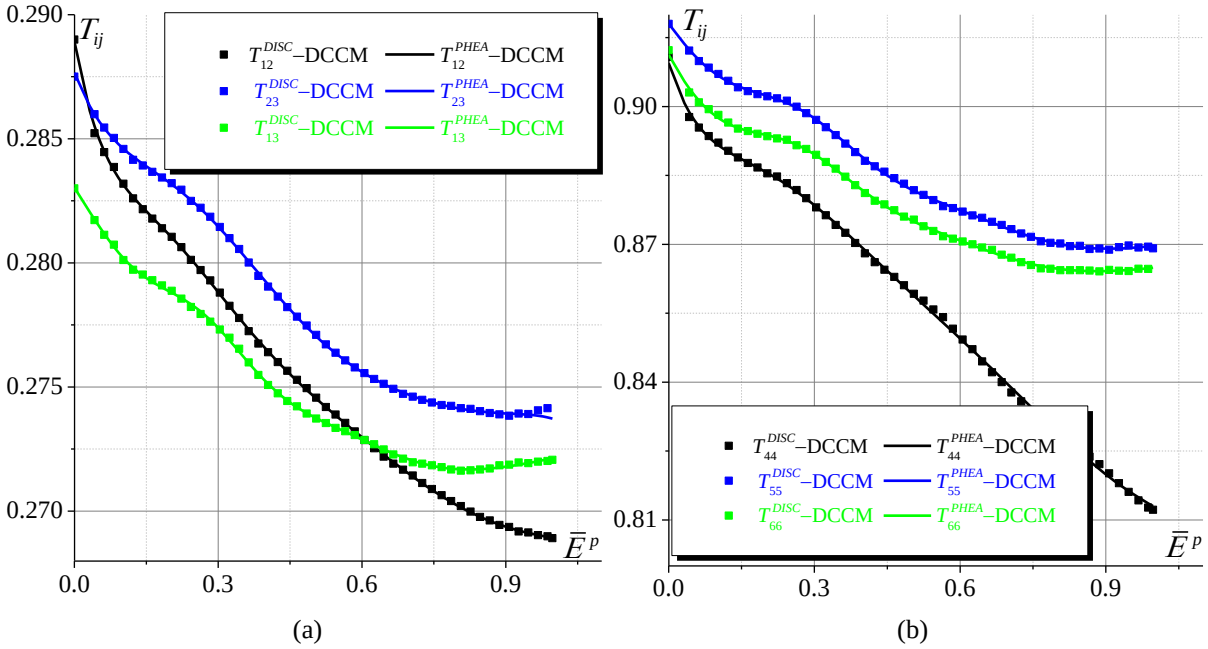

Fig. 8. Evolution of the anisotropy parameters (identification with DCCM): (a) Components T_{12}, T_{23}, and T_{13}, and (b) Components T_{44}, T_{55}, and T_{66}.

The values of the different fitting parameters, optimized with DCCM, are provided in Table 5.

Table 5. Identification of the fitting parameters (DCCM).

	A^1	A^2	k^1	A^3	A^4	A^5
T_{12}	-84.24	82.03	0.3326	27.23	-4.689	2.502
T_{13}	-35.26	33.57	0.4191	14.02	-3.052	1.976
T_{23}	-16.66	15.14	0.5294	7.972	-2.221	1.812
T_{44}	-1.487	0.1405	4.928	0.3897	-0.8177	2.264
T_{55}	-147.7	137.7	0.4729	64.90	-15.94	10.96
T_{66}	-200.6	191.1	0.4175	79.53	-17.15	10.54

One may again highlight here an undeniable advantage of the sequential identification of the material parameters: the identification of the yield loci explained in Section 3.2.3 provides the discrete (numerical) values of components T_{ij} for the different deformation levels. Then, the identification of the evolution laws of T_{ij} is managed separately from the previous identification steps. In particular, one can accurately fit the functions T_{ij} to their numerical evolutions identified in Section 3.2.3, as has been shown in Fig. 7 and Fig. 8. Simultaneous identification of all the parameters would have made unreadable the influence of the selected evolution functions for T_{ij}.

3.2.5. Improvement of the identification of the plastic anisotropy parameters considering non-associated flow rule aspects

To check the consistency of the previous identification steps, the evolution of the 'accumulated' Lankford coefficient $r_\beta = E_{22}^p / E_{33}^p$ versus the loading direction β obtained by the polycrystalline model is compared with its counterpart predicted by the phenomenological model (with evolving plastic anisotropy). The use of the 'accumulated' Lankford coefficient instead of the classical one (equal to $\dot{E}_{22}^p / \dot{E}_{33}^p$) is motivated by the strong fluctuation observed in the evolution of components $\dot{E}_{22}^p$ and $\dot{E}_{33}^p$ predicted by the polycrystalline model, which is mainly due to the fast changes in the activity of the CSSs at the grain level. Hence, the use of E_{22}^p and E_{33}^p instead of their rates allows providing a smoother evolution for the Lankford coefficient. In this comparative study, different accumulated plastic strain levels are considered: $\bar{E}^p = 0.1, 0.2, 0.3$. The trends are almost insensitive to the consideration or not of the damage evolution in the constitutive modeling. Hence, only the results obtained by DCCM are presented hereafter. As a first guess, the associated plasticity flow rule is used ($\underline{\phi} = \phi$, with parameters of ϕ and their evolution laws determined by the identification procedures of Sections 3.2.3 and 3.2.4). As revealed by Fig. 9, the polycrystalline trends are globally reproduced by the associated phenomenological model (with evolving plastic anisotropy). However, the peak of the Lankford coefficient, observed for a loading direction β of about $45°$, is largely underestimated by the associated phenomenological model.

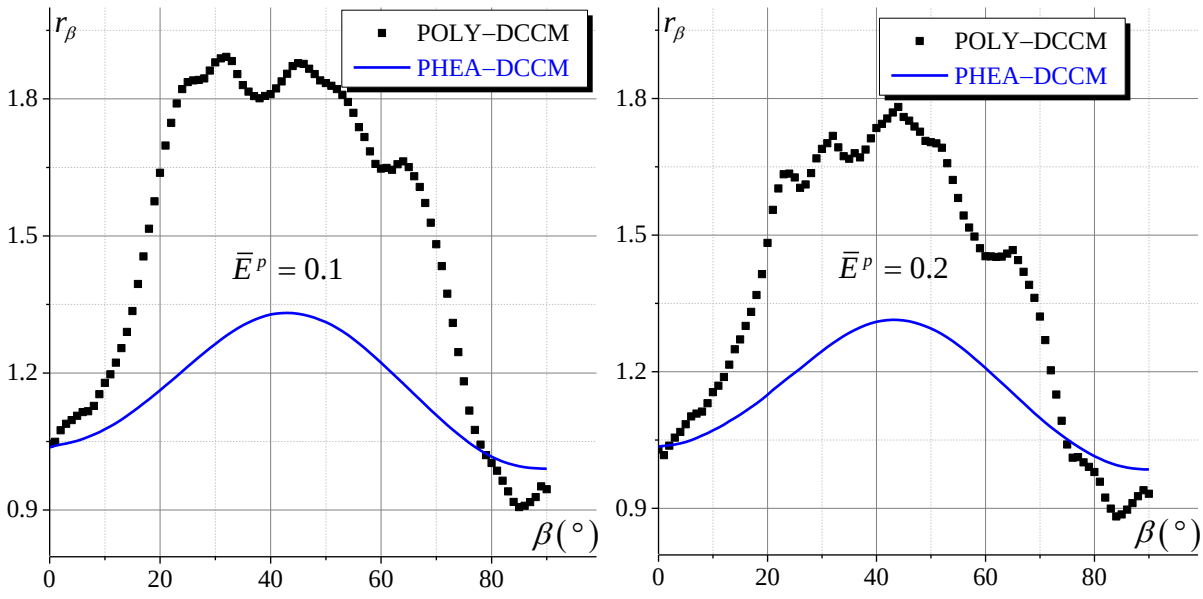

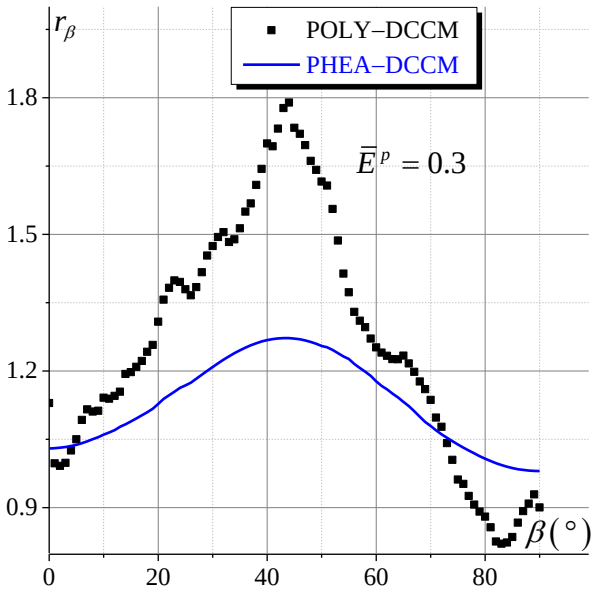

(c)

Fig. 9. Evolution of the Lankford coefficient r_β versus the loading direction β using associated flow rule ($\underline{\phi} = \phi$) and DCCM for: (a) $\bar{E}^p = 0.1$, (b) $\bar{E}^p = 0.2$, and (c) $\bar{E}^p = 0.3$.

The results displayed in Fig. 9 reveal that the anisotropy of the yield surface and the plastic flow (described by the evolution of the Lankford coefficients) are quite different. Indeed, the associated version of the phenomenological model allows correctly fitting the yield surface; however, it shows some limitations in accurately fitting the Lankford coefficients. To improve the optimization of the anisotropy parameters, the non-associated general model (i.e. $\underline{\phi} \neq \phi$) is used in the identification procedure. Within this non-associated model, the anisotropy parameters $\mathcal{P}_\phi$ corresponding to the yield function ϕ are kept to their values and evolutions identified in Sections 3.2.3 and 3.2.4. Furthermore, the components $\underline{T}_{ij}$ are assumed to be equal to T_{ij}. This assumption, which allows considerably simplifying the identification of the non-associated anisotropy parameters, is relevant as we have observed that the Lankford coefficients are almost independent of the components of the transformation matrix $\underline{\mathbb{T}}$. On the other hand, we have varied the value of the exponent parameter $\underline{A}$ to reach the best fit of the non-associated phenomenological parameters from the polycrystalline predictions. After a quick parametric study, we have concluded that the exponent $\underline{A}$ should be around 22 to obtain the best fit. The comparisons between the polycrystalline simulations and the non-associated phenomenological model obtained with $\underline{A} = 22$ are displayed in Fig. 10. It is clearly shown in this figure that the fit of the results is quite enhanced in an average sense. This change in the flow rule leads to a slight modification for the evolution of the yield loci (Eqs. (16), (17) and (18)). After

checking the phenomenological predictions, we have observed that the exponent parameter $\underline{A}$ does not significantly impact the yield loci. In the validation section (Section 4), the non-associated flow rule is commonly used in all the predictions. The parameters of this non-associated flow rule are summarized in the following lines:

- The hardening and damage parameters are given in Table 2 for DUCM and Table 3 for DCCM.
- The components of the transformation matrix $\mathbb{T}$, which are equal to those of $\underline{\mathbb{T}}$, are given in Table 4 for DUCM and Table 5 for DCCM.
- Independently of the modeling approach, coupled or not with damage (i.e., DUCM or DCCM), exponents A and $\underline{A}$ are set to 9 and 22, respectively.

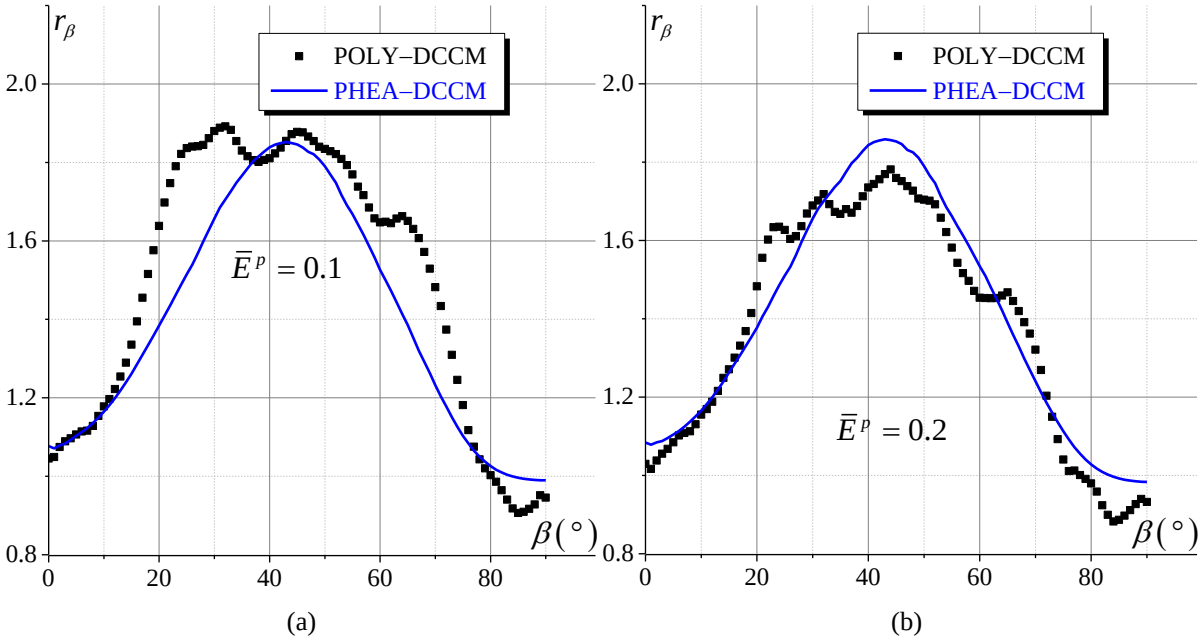

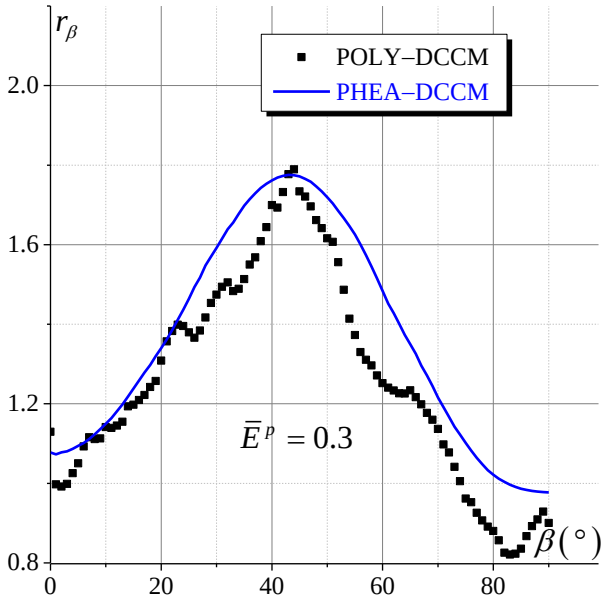

(c)

Fig. 10. Evolution of the Lankford coefficient r_β versus the loading direction β using non-associated flow rule ($A = 9$, $\underline{A} = 22$) and DCCM for: (a) $\bar{E}^p = 0.1$, (b) $\bar{E}^p = 0.2$, and (c) $\bar{E}^p = 0.3$.

4. Validation of the developed models

The capability of the developed phenomenological model to accurately reproduce the polycrystalline response is assessed through the simulation of a complex loading applied on a thin specimen, where a large number of finite elements is involved and the mechanical state is not homogeneous over the structure. The plane dimensions of this structure are detailed in Fig. 11a and its initial thickness is set to 0.4 mm. This specimen is subjected to a combined tensile/shear loading, as demonstrated in Fig. 11b. As shown in the same figure, this combined loading is the result of the specific geometry of the specimen and the applied boundary conditions: the lower side is fixed and the upper side is subjected to a vertical displacement denoted U_2, while the displacement in direction 1 (transverse direction) is fixed ($U_1 = 0$). The force required to induce the displacement U_2 is noted F_2, while the reaction force required to fix the lower side of the specimen in the horizontal direction is noted F_1. Direction 1 (resp. 2) shown in Fig. 11b is parallel to the transverse (resp. rolling) direction. This specimen is discretized with 3195 C3D8R finite elements, as illustrated in Fig. 11c. The mesh is refined near the central zone of the sheet, where large strain gradients are expected. Whereas, much coarser discretization is used in the rest of the specimen, where a rather uniform deformation is expected. To consider the effect of the out-of-plane strain, three element layers have been used along the sheet thickness. As well known, accounting for the full coupling with ductile damage in the framework of local formulation leads to

mesh dependence pathology. Several solutions have been proposed in the literature to overcome this pathology, such as the use of nonlocal formulations with gradient plasticity models [71–73], and micromorphic formulations [74–75]. The dependency of the numerical predictions on the mesh discretization is not analyzed in the current paper, as it will be the subject of a future investigation. To reduce the length of the paper, only the DCCM has been used to obtain the predictions of this Section, where four types of simulations have been performed:

- Simulations with the phenomenological model, where the evolution of anisotropy parameters is not considered (PHIA). In this case, the anisotropy parameters are fixed to their initial values easily determined from Fig. 8:

$$T_{12}=0.289,\quad T_{23}=0.287,\quad T_{13}=0.283,\quad T_{44}=0.911,\quad T_{55}=0.918,\quad T_{66}=0.912. \tag{51}$$

- Simulations with the phenomenological model, where the anisotropy parameters are assumed to evolve according to the evolution law of Eq. (46) and the curves of Fig. 8 (PHEA).
- Simulations with the self-consistent polycrystalline model (POLY).
- Simulation using a hybrid FE approach (HYBR): this hybrid approach consists in the combination of phenomenological (with evolving anisotropy) and multiscale approaches within the same FE model: the phenomenological model (PHEA) has been assigned to the weakly loaded zone of the specimen (called calm zone). However, the multiscale approach (POLY) has been assigned to the zone exhibiting a strong evolution of plastic flow (called critical zone). The critical zone is colored in red in Fig. 11c. The FE simulation based on the phenomenological modeling has been used to identify both zones and the interface between them. The partition of the specimen is illustrated in Fig. 11c, where the calm zone is colored in grey and the critical zone is colored in red. The same mesh as the one presented in Fig. 11c is used in this hybrid simulation, where 300 C3D8R solid elements have been assigned to the critical zone.

In these simulations, the final displacement U_2 of the upper boundary of the specimen is fixed to $0.4\,mm$, which corresponds approximatively to the macroscopic failure initiation (numerically detected at the integration point where the damage variable D reaches the critical value of 0.9). In the numerical predictions, particular attention will be paid to the evolution of the mechanical behavior in two material points: point N°1 located in the center of the specimen and point N°2 laid in the boundary (surface) of the specimen, as demonstrated in Fig. 11c.

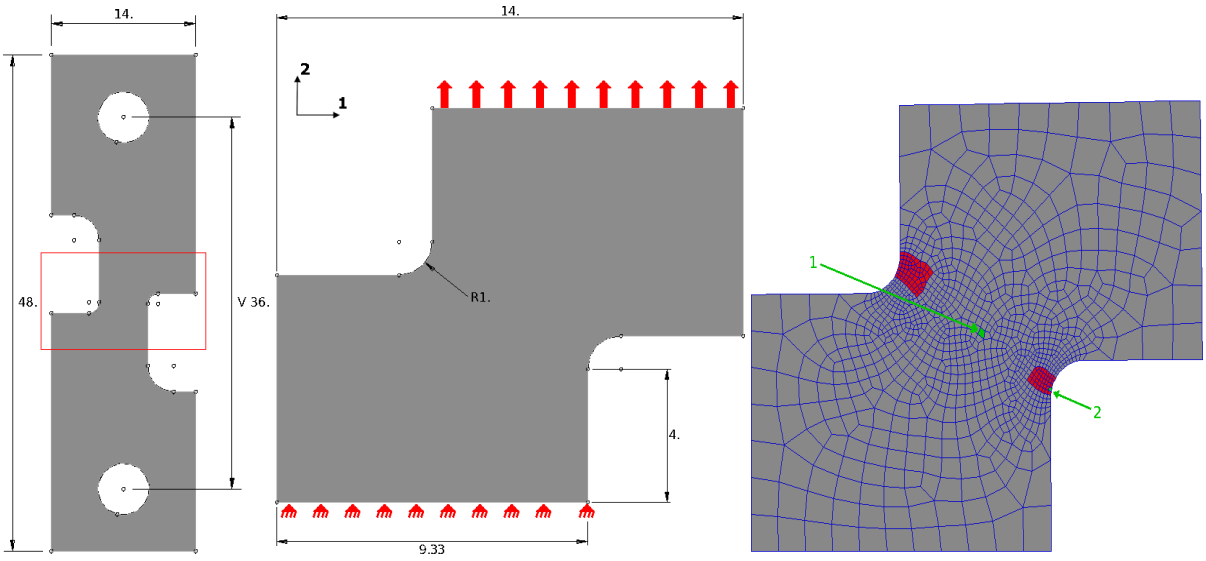

(a) (b) (c)

Fig. 11. Simulation of the combined tensile/shear test: (a) Geometry and dimensions of the specimen, (b) Geometry of the useful zone and applied boundary conditions, and (c) FE mesh and reference to the studied points (the zones colored in red refer to the critical zones modeled by the POLY model).

The CPU time required to run each of the two first simulations (based on PHIA and PHEA models) on one core is about 30 minutes. However, the third simulation (with the POLY model) has required approximately 120 hours on 32 computational cores. On the other hand, the last simulation based on the hybrid strategy (HYBR) has taken 40 hours on 32 computational cores. This comparison confirms the large advantage, in terms of computational efficiency, of phenomenological as well as hybrid modeling compared to the polycrystalline one.

The evolutions of forces F_1 and F_2 versus the vertical displacement U_2 obtained by the different models are reported in Fig. 12. As clearly shown in Fig. 12a, the curves providing the force component F_2 obtained by the different simulations are almost indistinguishable when the force level is less than the maximum value, for which the damage value and its evolution remain low. However, when the damage evolution accelerates, the different predictions become quite different. Note that the force level obtained by the hybrid model leads to the best fit compared to the polycrystalline one. This hybrid model yields predictions that are comprised between those obtained by the polycrystalline and phenomenological models. This result is expectable, as the hybrid strategy is a combination of the other models. On the other hand, the evolution of the force component F_2 obtained by the phenomenological model with evolving anisotropy is closer to its counterpart predicted by the polycrystalline model than the evolution obtained without evolving anisotropy. This comparison demonstrates once again the importance of accounting for plastic anisotropy evolution. The evolutions

of the force component F_1 displayed in Fig. 12b globally confirm the trends obtained with the force F_2. Those results confirm the benefits of the two introduced novelties: the evolving anisotropy and the hybrid simulation method, both significantly contributing to more closely approaching the polycrystalline model predictions. It is important to mention that the polycrystalline model predicts the highest force level, and leads to the lowest damage evolution and softening (as will be confirmed by the curves of Fig. 17). By contrast, the use of the PHIA model leads to the lowest force level with the highest damage evolution and softening (see Fig. 17). The difference between these trends corroborates the idea that accounting for evolving anisotropy tends to promote the material hardening, which in turn reduces the softening evolution. This can be explained, for the polycrystalline model, by the fact that as the loading increases, the grains rotate leading to an increase in the number of active slip systems. Such an increase in CSS activity induces more accumulated plastic strain, which tends to promote the material hardening. However, the new activated slip systems will not increase further the average damage level in the polycrystalline aggregate.

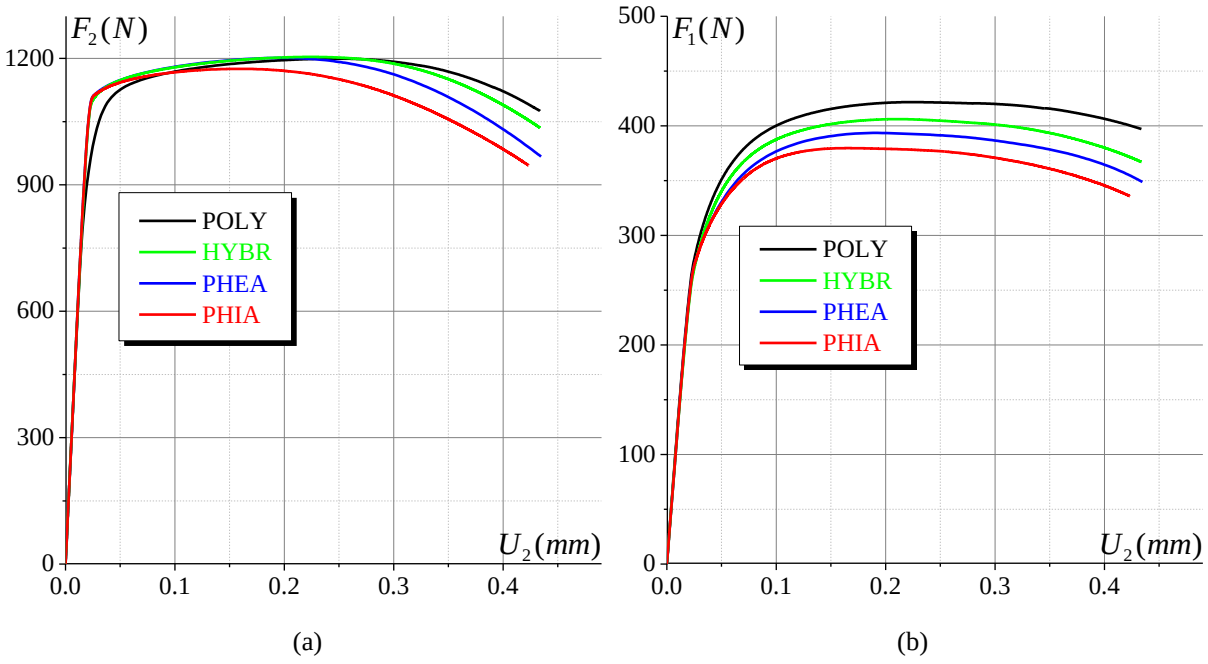

Fig. 12. Evolution of the global forces as functions of the vertical displacement (simulations with DCCM): (a) Force F_2, and (b) Force F_1.

The distributions of the maximum logarithmic strain, the von Mises equivalent stress, and the damage variable (D or D^{POLY}, depending on the adopted model) over the specimen, as predicted at $U_2 = 0.4mm$ by the different models, are reported in Fig. 13, Fig. 14, and Fig. 15, respectively. As shown from these isovalues, the different models yield close responses on the whole. Careful observation of the strain isovalues presented in Fig. 13 reveals slightly more pronounced localization

predicted by the polycrystalline model. The hybrid computation better reproduces this phenomenon than both phenomenological models, with closer predicted strain values. As can be observed, the PHEA model leads to more accurate predictions of the localization zone (closer to the polycrystalline predictions), as compared to the more classical PHIA model. This result confirms the better predictive capabilities of the PHEA model compared to the PHIA one.

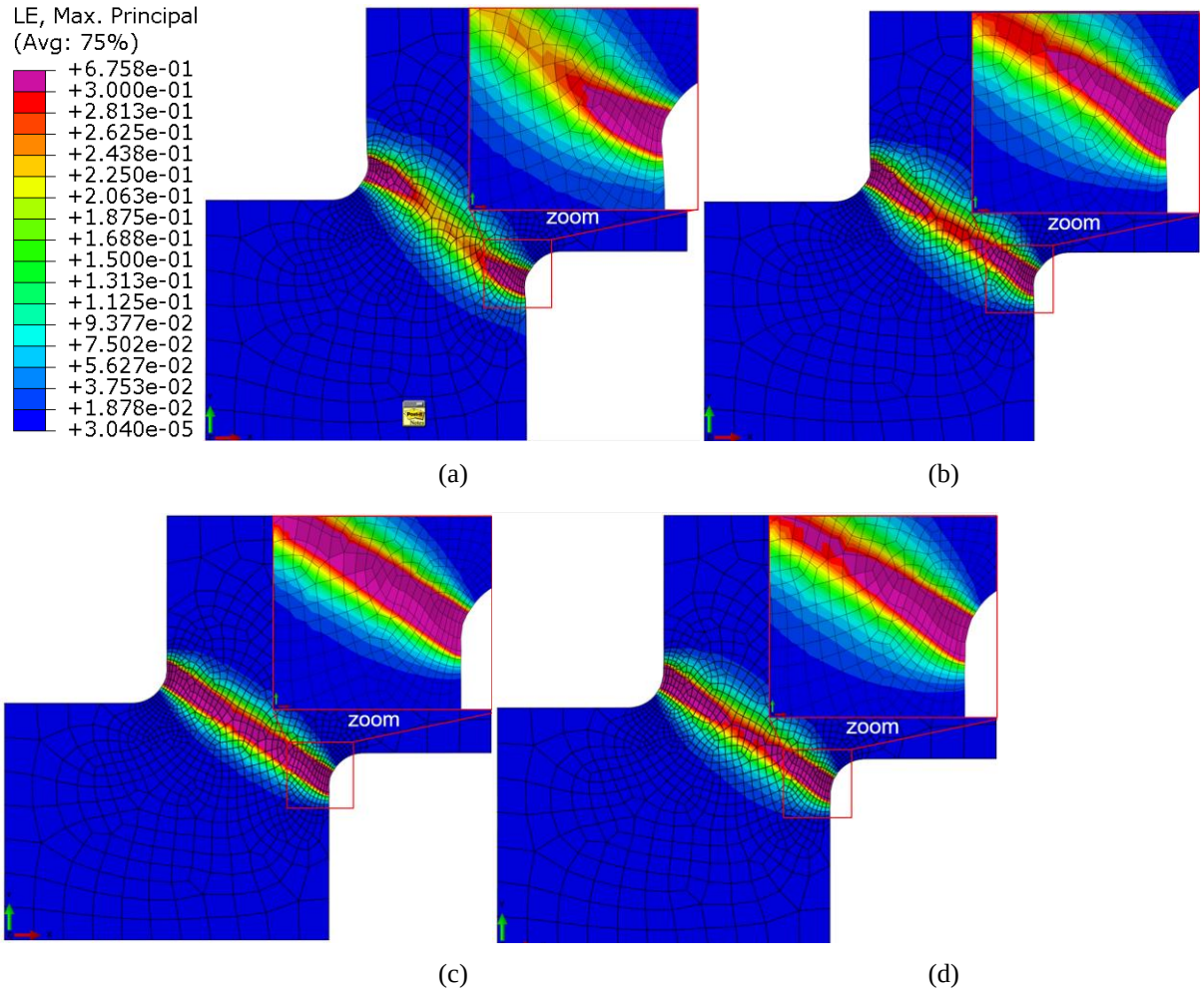

Fig. 13. Contour plot of the maximum logarithmic strain predicted at $U_2 = 0.4\ mm$ using: (a) POLY model, (b) HYBR model, (c) PHIA model, and (d) PHEA model.

The stress maps (Fig. 14) also show better accordance between hybrid and polycrystalline computations, while both phenomenological computations show early stress weakening in the critical zone. This early weakening can be explained by difficulty to reproduce the polycrystalline model when damage becomes significant, as already explained in Section 3.2.3**.** Closer observation of the local behavior in the critical zone (point N°2) is provided hereafter to better understand this phenomenon. The hybrid computation confirms here its ability to overcome the difficulty to reproduce the polycrystalline behavior when damage becomes significant.

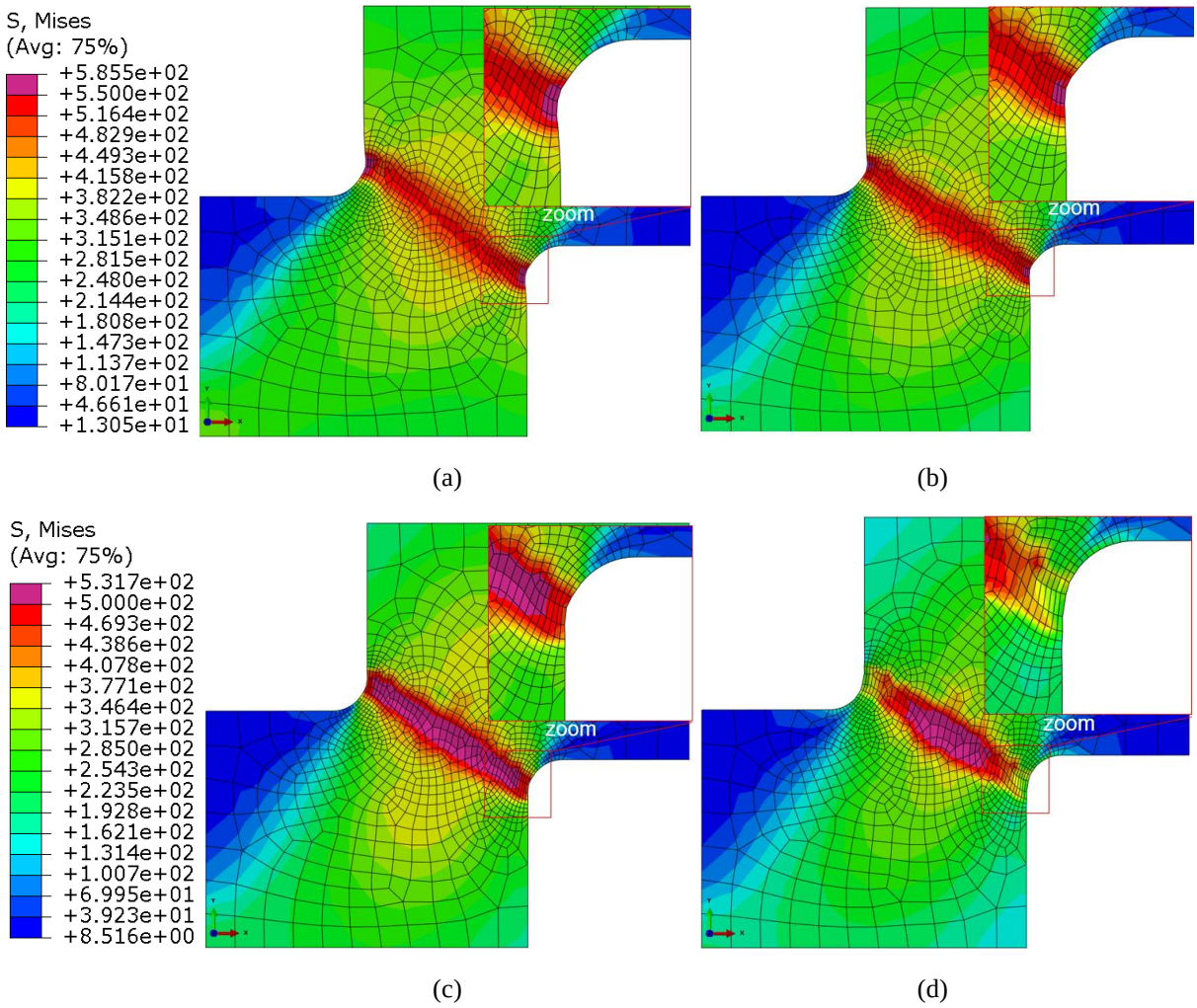

Fig. 14. Contour plot of the von Mises equivalent stress predicted at $U_2 = 0.4\ mm$ using: (a) POLY model, (b) HYBR model, (c) PHIA model, and (d) PHEA model.

As shown in Fig. 15, the localization of the damage variables D^{POLY} and D, as predicted by the different models, follows a similar trend on the whole. In particular, the maps of D^{POLY} obtained by the polycrystalline and hybrid computations are relatively close (one recalls that, in Fig. 15b, the isovalues correspond to D^{POLY} in the critical area and D elsewhere, thus the comparison should be restricted to the critical area). Also, the discontinuity that appears at the boundary between the critical and calm areas is not significant: it corresponds to the incompatibility between D^{POLY} and D explained in Section 3.2.2 (see Fig. 4). For the phenomenological models, one can observe, as explained before, that the PHIA model induces faster damage evolution, which affects strongly the mechanical behavior. Since we have previously concluded (see Fig. 15) that both phenomenological models predict too fast stress weakening in the critical area, a slower damage evolution seems more relevant. In addition, both phenomenological models poorly reproduce the polycrystalline model predictions in the damaged area, thus pointing out the relevance of the hybrid strategy for the accurate modeling of critical areas

exhibiting highly deformed zones with localization of plastic flow and damage.

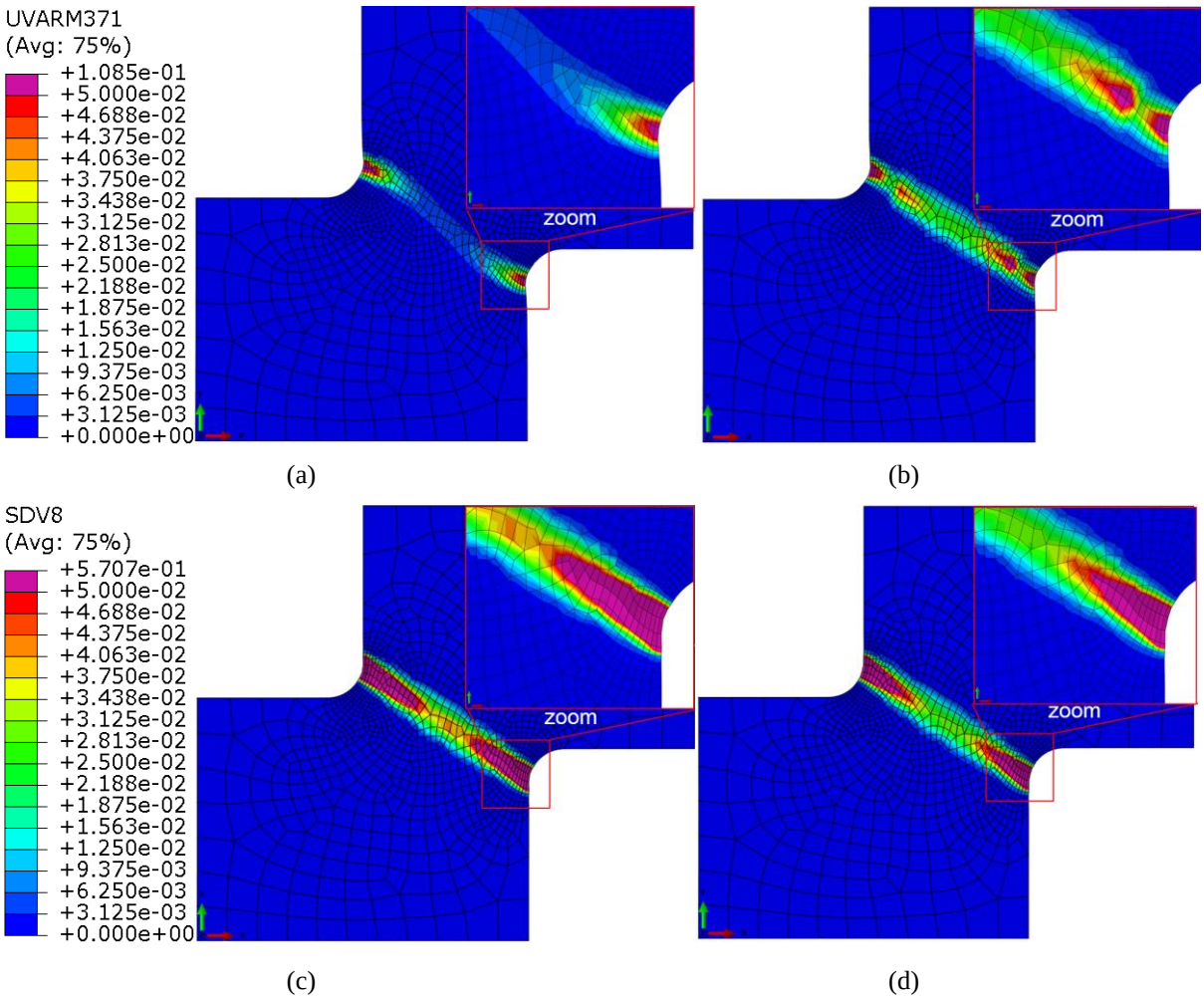

Fig. 15. Contour plot of the macroscopic damage variable predicted at $U_2 = 0.4\ mm$ using: (a) POLY model, (b) HYBR model, (c) PHIA model, and (d) PHEA model.

Considering now closer (local) observation at the material points N°1 and N°2 (the positions of these points are indicated in Fig. 11c), one observes good agreement between the predictions obtained by the four models in terms of stress components Σ_{11} and Σ_{12} versus the displacement U_2, as long as the displacement (and hence damage) remains small ($U_2 < 0.2\ mm$), as illustrated in Fig. 16.

For the material point N°1, in which the amount of damage does not reach an important value, as shown in Fig. 17a, the gap between the stress components predicted by the different models remains small for all the simulations. However, for point N°2, where the damage evolution becomes important (Fig. 17b), the difference between the predictions of the three models is much more noticeable. At this stage of damage evolution, the predictions of the phenomenological models (with and without anisotropy evolution) significantly differ from those of the polycrystalline model. Recall that early

weakening of the stress occurred for both phenomenological models. This confirms the difficulty in describing the damage behavior of the polycrystalline aggregate with the proposed phenomenological model, as already pointed out in Section 3.2.3. On that scope, the hybrid simulations provide better results (point N°2, Fig. 17b). The predicted damage variables D^{POLY} also remain close for both polycrystalline and hybrid computations. This confirms the reliability of the hybrid strategy to predict the complex behavior of polycrystalline aggregates in critical zones.

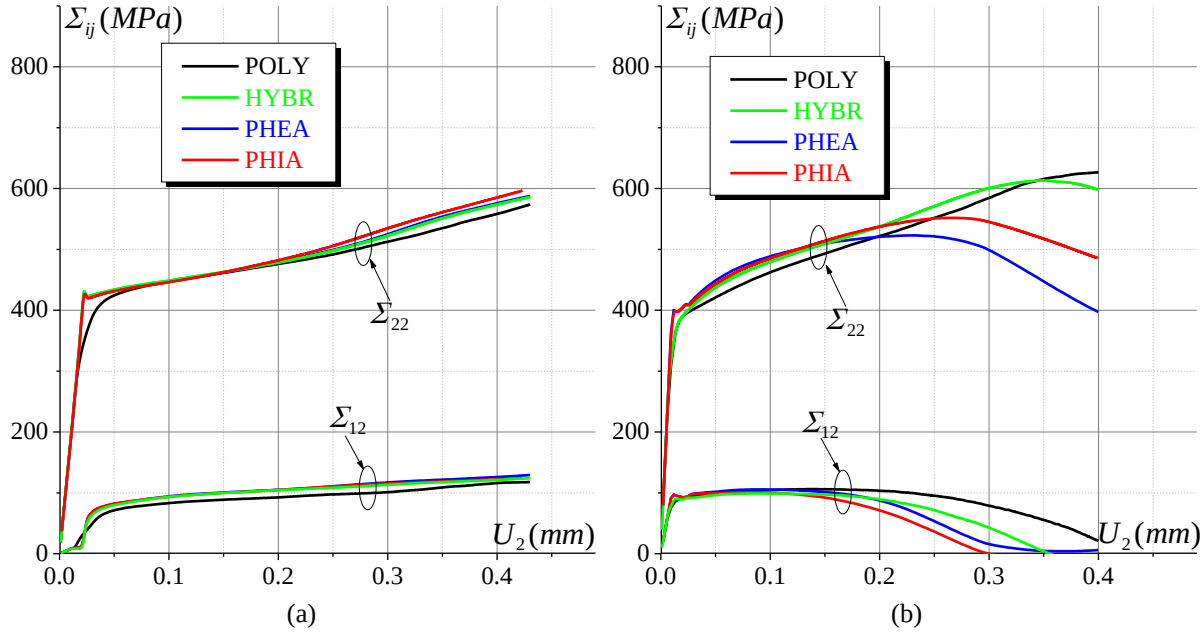

Fig. 16. Evolution of the stress components Σ_{11} and Σ_{12} versus the displacement U_2 (DCCM): (a) point N°1, and (b) point N°2.

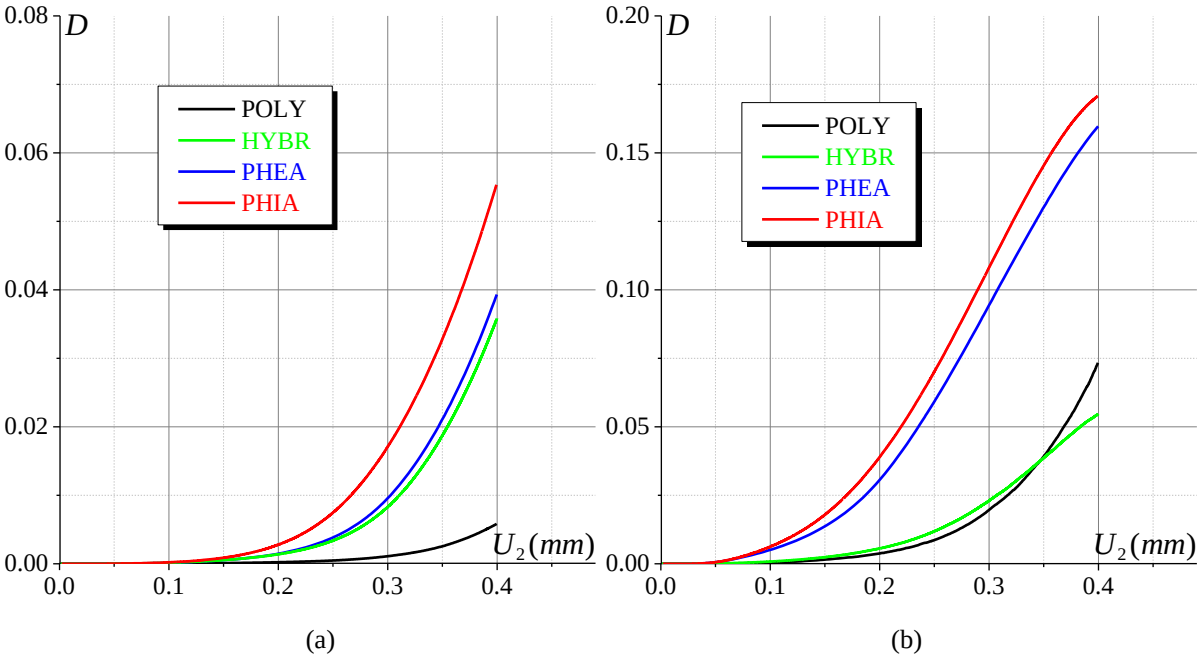

Fig. 17. Evolution of the damage variables D^{POLY} and D in two points of the sheet. (a) Point N°1 (D^{POLY} for POLY model; D for the three others), and (b) Point N°2 (D^{POLY} for POLY and HYBR models; D for PHIA and PHEA models).

The observed differences between predictions obtained by POLY and HYBR models in the critical area (highlighted in red in Fig. 11c), where both simulations use the polycrystalline model, is the result of differences in terms of strain localization within the sheet. Indeed, the hybrid simulation uses the PHEA model in the calm area, while the polycrystalline simulation uses the polycrystalline model everywhere, thus leading to different strain localization within the whole sheet, including the critical area. Figure 18 shows the evolution of the strain components E_{22} and E_{12} at point N°2 (in the critical area), as predicted by each computation, thus highlighting that the use of the phenomenological model within the hybrid simulation influences the strain localization, even in the critical area. In that regard, the strain predicted by the hybrid simulation at point N°2 appears to be closer to the strain obtained by both phenomenological simulations than to the strain predicted by the polycrystalline model, explaining the imperfect accordance in the stress evolution observed in Fig. 16b. However, this difference remains reasonable and only concerns the critical area under high damage values, while global accordance between polycrystalline and hybrid simulations is satisfactory.

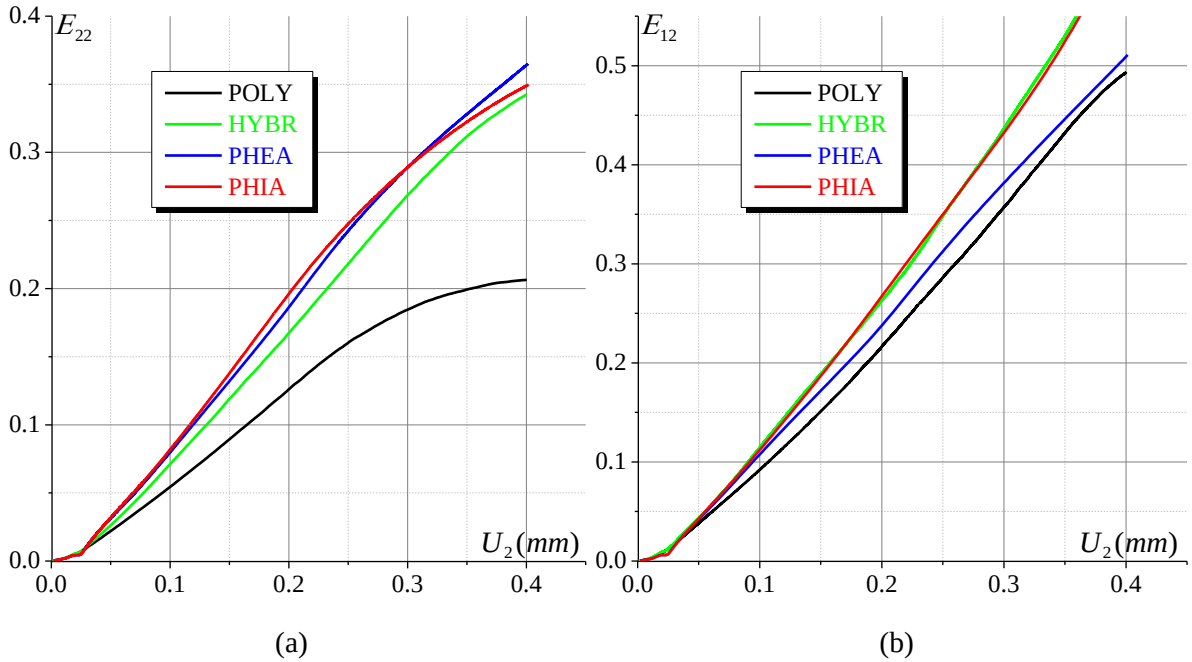

Fig. 18. Evolution of the relevant strain components at point N°2: (a) Component E_{22}, and (b) Component E_{12}.

5. Conclusions

In this paper, an advanced phenomenological model has been developed to accurately reproduce the mechanical responses predicted by the multiscale crystal plasticity scheme developed in [45]. In both models (namely, single-scale and multiscale), the behavior is assumed to be elastoplastic (rate-independent) and the constitutive equations are formulated under finite strain assumption. Compared to recent investigations devoted to the same kind of modeling, the current investigation presents an important novelty: the effect of damage evolution on the mechanical behavior is accounted for in both constitutive models. The different constitutive equations have been implemented into ABAQUS/Standard finite element (FE) code as user material (UMAT) subroutines. To accurately reproduce the evolution of plastic anisotropy, induced by the evolution of crystallographic texture, a pragmatic methodology has been developed and implemented into the advanced phenomenological model. Within this methodology, the anisotropy parameters have been assumed to evolve during the plastic loading. The procedures developed to identify the macroscopic material parameters and their eventual evolutions have been extensively discussed. Several numerical predictions have been presented to assess the reliability of the developed models. It turns out from these predictions that the developed advanced model, though with relatively small defects in the modeling of damage evolution, may be a promising way to accurately and efficiently model the mechanical behavior during sheet metal forming.

To enhance its accuracy in the prediction of polycrystalline behavior, the advanced model should be extended in future investigations to include the following aspects:

- The anisotropy of the damage evolution in both constitutive models using tensor representation of the damage variables, instead of the scalar variables used here.
- The distortional hardening in the phenomenological model using the homogeneous anisotropic hardening (HAH) approach.
- The use of a micromorphic formulation in order to avoid the mesh dependency pathology.

The developed numerical tools shall be validated and improved using extensive experimental database containing different experimental tests results.

Acknowledgments

This work has been carried out within the research project RESEM 2019, managed by the *Institut de Recherche Technologique Matériaux Métallurgie Procédés (IRT M2P)* and financially supported by the *French program Plan d'Investissement d'Avenir (PIA)*.

References

1 Hill, R., 1948. A theory of the yielding and plastic flow of anisotropic metals. Proc. Roy. Soc. A 193, 281–297.

2 Karafillis, A.P., Boyce, M.C., 1993. A general anisotropic yield criterion using bounds and a transformation weighting tensor. J. Mech. Phys. Solids 41, 1859–1886.

3 Barlat, F., Brem, J.C., Yoon, J.W., Chung, K., Dick, R.E., Lege, D.J., Pourboghrat, F., Choi, S.-H., Chu, E., 2003. Plane stress yield function for aluminum alloy sheets – Part I: theory. Int. J. Plast. 19, 1297–1319.

4 Cazacu, O., Barlat, F., 2004. A criterion for description of anisotropy and yield differential effects in pressure insensitive metals. Int. J. Plast. 20, 2027–2045.

5 Banabic, D., Kuwabara, T., Balan, T., Comsa, D.S., Julean, D., 2003. Non-quadratic yield criterion for orthotropic sheet metals under plane-stress conditions. Int. J. Mech. Sci. 45, 797–811.

6 Yoon, J.W., Barlat, F., Dick, R.E., Karabin, M.E., 2006. Prediction of six or eight ears in a drawn cup based on a new anisotropic yield function. Int. J. Plast. 22, 174–193.

7 Khan, A.S., Kazmi, R., Pandey, A., Stoughton T., 2009. Evolution of Subsequent Yield Surfaces and Elastic Constants with Finite Plastic Deformation, Part-I: A Very Low Work Hardening Aluminum Alloy (6061-T6511). Int. J. Plast. 25, 1611–1625.

8 Kuroda, M., Tvergaard, V., 2000. Forming Limit Diagrams for Anisotropic Metal Sheets with Different Yield Criteria. Int. J. Solids Struct. 37, 5037–5059.

9 Abedrabbo, N., Pourboghrat, F., Carsley, J., 2006. Forming of aluminum alloys at elevated temperatures – Part 1: Material characterization. Int. J. Plast. 22, 314–341.

10 Aretz, H., 2008. A simple isotropic-distortional hardening model and its application in elastic–plastic analysis of localized necking in orthotropic sheet metals. Int. J. Plast. 24,1457–1480.

11 Stoughton, T.B., Yoon, J.W., 2009. Anisotropic Hardening and Non-Associated Flow in Proportional Loading of Sheet Metals. Int. J. Plast. 25, 1777–1817.

12 Kuroda, M., Tvergaard, V., 2001. A phenomenological plasticity model with non-normality effects representing observations in crystal plasticity. J. Mech. Phys. Solids 49, 1239–1263.

13 Chung, K., Lee, M.G., Kim, D., Kim C.K., Wenner, M.L., Barlat, F., 2005. Spring-back evaluation of automotive sheets based on isotropic-kinematic hardening laws and non-quadratic anisotropic yield function; Part I: Theory and Formulation. Int. J. Plast. 21, 861–882.

14 Cvitanic, V., Vlak, F., Lozina, Z., 2008. A finite element formulation based on non-associated plasticity for sheet metal forming. Int. J. Plast. 24, 646–687.

15 Taherizadeh, A., Green, D.E., Gahei, A., Yoon, J.W., 2010. A non-associated constitutive model with mixed iso-kinematic hardening for finite element simulation of sheet metal forming. Int. J. Plast. 26 (2), 288–309.

16 Barlat, F., Gracio, J.J., Lee, M.-G., Rauch, E.F., Vincze, G., 2011. An alternative to kinematic hardening in classical plasticity. Int. J. Plast. 27 (9), 1309–1327.

17 Barlat, F., Ha, J., Gracio, J.J., Lee, M.-G., Rauch, E.F., Vincze, G., 2013. Extension of homogeneous anisotropic hardening model to cross-loading with latent effects. Int. J. Plast. 46, 130–142.

18 Barlat, F., Vincze, G., Grácio, J.J., Lee, M.-G., Rauch, E.F., Tomé, C.N., 2014. Enhancements of homogenous anisotropic hardening model and application to mild and dual-phase steels. Int. J. Plast. 58, 201–218.

19 Brünig, M., 2003. An anisotropic ductile damage model based on irreversible thermodynamics. Int. J. Plast. 19, 1679–1713.

20 Lemaitre, J., Chaboche, J.L., Benallal, A., Desmorat, R., 2009. Mécanique des matériaux solides. Dunod, Paris. 3ème éditions.

21 Badreddine, H., Saanouni, K., Dogui, A., 2010. On non-associative anisotropic finite plasticity fully coupled with isotropic ductile damage for metal forming. Int. J. Plast. 26, 1541–1575.

22 Saanouni, K., 2012. Damage Mechanics in metal forming. Advanced modeling and numerical simulation, ISTE/Wiley, London, ISBN: 978–1–84821–3487.

23 Yue, Z.M., Badreddine, H., Saanouni, K., Perdahcioglu, E.S., 2017. Experimental and numerical studies of AL7020 formability under orthogonal loading paths with considering yield surface distortion. Int. J. Mech. Sci. 123, 151–161.

24 François, M., 2001. A plasticity model with yield surface distortion for non-proportional loading. Int. J. Plast. 17, 703–717.

25 Badreddine, H., Saanouni, K., 2017. On the full coupling of plastic anisotropy and anisotropic ductile damage under finite strains. Int. J. Damage Mech. 26 (7), 1080–1123.

26 Helling, D.E., Miller, A.K., 1987. The incorporation of yield surface distortion into a unified constitutive model, part 1: Equation development. Acta Mech. 69, 9–23.

27 Voyiadjis, G.Z., Foroozesh, M., 1990. Anisotropic distortional yield model. J. Appl. Mech. 57, 537–547.

28 Voyiadjis, G., Thiagarajan, G., Petrakis, E., 1995. Constitutive modelling for granular media using an anisotropic distortional yield model. Acta Mech. 110, 151–171.

29 Feigenbaum, H.P., Dafalias, Y.F., 2007. Directional distortional hardening in metal plasticity within thermodynamics. Int. J. Solids Struct. 44, 7526-7542.

30 Kachanov, L. M., 1986. Introduction to Continuum Damage Mechanics. Netherlands, Martinus Nijhoff Publishers.

31 Murakami, S., 1988. Mechanical modeling of material damage. J. Appl. Mech. 55 (2), 280–286.

32 Lemaitre, J., 1992. A Course on Damage Mechanics. Springer, Berlin.

33 Chaboche, J.L., 1999. Thermodynamically founded CDM models for creep and other conditions: CISM courses and lectures No 399, International Centre for Mechanical Sciences. Creep Damage Mater. Struct., 209–283.

34 Voyiadjis, G.Z., Kattan, P.I., 1999. Advances in Damage Mechanics: Metals and Metal Matrix Composites. Elsevier Oxford, UK.

35 Saanouni, K., Chaboche, J.L., 2003. Computational damage mechanics. Application to metal forming. Chapter 7 of Vol. 3 “Numerical and Computational methods”, Ed. I. Milne, R.O. Ritchie and B. Karihaloo, ISBN 0–08–043749–4, Elsevier Oxford (UK), 321–376.

36 Barros, P.D., Alves, J.L., Oliveira, M.C., Menezes, L.F., 2016. Modeling of tension–compression asymmetry and orthotropy on metallic materials: Numerical implementation and validation. Int. J. Mech. Sci. 114, 217–232.

37 Li, H., Hu, X., Yang, H., Li, L., 2016. Anisotropic and asymmetrical yielding and its distorted evolution: Modeling and applications. Int. J. Plast. 82, 127–158.

38 Kabirian, F., Khan, A.S., Gnäupel-Herlod, T., 2016. Plastic deformation behavior of a thermo-mechanically processed AZ31 magnesium alloy under a wide range of temperature and strain rate. J. Alloys Compd. 673, 327–335.

39 Lee, M.G., Wagoner, R.H., Lee, J.K., Chung, K., Kim, H.Y., 2008. Constitutive modeling for anisotropic/asymmetric hardening behavior of magnesium alloy sheets. Int. J. Plast. 24, 545–582.

40 Taylor, G.I., 1938. Plastic strain in metals. Journal of Institution of Metals 62, 307–324.

41 Bishop, J.F.W., Hill, R., 1951. A theory of the plastic distortion of a polycrystalline aggregate under combined stresses. Philosophical Magazine 42, 414–427.

42 Bishop, J.F.W., Hill, R., 1951. A theoretical derivation of the plastic properties of a face-centred metal. Philosophical Magazine 42, 1298–1307.

43 Knezevic, M., Kalidindi, S.R., Fullwood, D., 2008. Computationally efficient database and spectral interpolation for fully plastic Taylor-type crystal plasticity calculations of face-centered cubic polycrystals. Int. J. Plast. 24 (7), 1264–1276.

44 Knezevic, M., Al-Harbi, H.F., Kalidindi, S.R., 2009. Crystal plasticity simulations using discrete Fourier transforms. Acta. Mater. 57 (6), 1777–1784.

45 Paux, J., Ben Bettaieb, M., Badreddine, H., Abed-Meraim, F., Labergere, C., Saanouni, K., 2020. An elasto-plastic self-consistent model for damaged polycrystalline materials: Theoretical formulation and numerical implementation. Comput. Methods Appl. Mech. Engrg. 368, 113138.

46 Lipinski, P., Berveiller, M., 1989. Elastoplasticity of micro-inhomogeneous metals at large strains. Int. J. Plast. 5, 149–172.

47 Akpama, H.K., Ben Bettaieb, M., Abed-Meraim, F., 2017. Localized necking predictions based on rate-independent self-consistent polycrystal plasticity: Bifurcation analysis versus imperfection approach. Int. J. Plast. 91, 205–237.

48 Knezevic, M., Zecevic, M., Beyerlein, I.J., Lebensohn, R.A., 2016. A numerical procedure enabling accurate descriptions of strain rate-sensitive flow of polycrystals within crystal visco-plasticity theory. Comput. Methods Appl. Mech. Eng. 308, 468–482.

49 Akpama, H.K., Ben Bettaieb, M., Abed-Meraim, F., 2017. Prediction of plastic instability in sheet metals during forming processes using the loss of ellipticity approach. Lat. Am. J. Solids Struct. 14, 1816–1836.

50 Zecevic, M., Lebensohn, R.A., McCabe, R.J., Knezevic, M., 2019. Modelling recrystallization textures driven by intragranular fluctuations implemented in the viscoplastic self-consistent formulation. Acta. Mater. 164, 530–546.

51 Temizer, I., Wriggers, P., 2011. An adaptive multiscale resolution strategy for the finite deformation analysis of microheterogeneous structures. Comput. Methods Appl. Mech. Eng. 200, 2639–2661.

52 Coenen, E., Kouznetsova, V., Bosco, E., Geers, M., 2012. A multi-scale approach to bridge microscale damage and macroscale failure: a nested computational homogenization-localization framework. Int. J. Fract. 178, 157–178.

53 Reis, F.J.P., Andrade Pires, F.M., 2013. An adaptive sub-incremental strategy for the solution of homogenization-based multi-scale problems. Comput. Methods Appl. Mech. Eng. 257, 164–182.

54 Plunkett, B., Lebensohn, R.A., Cazacu, O., Barlat, F., 2006. Evolving yield function of hexagonal materials taking into account texture development and anisotropic hardening. Acta Mater. 54, 4159–4169.

55 Grytten, F., Holmedal, B., Hopperstad, O.S., Borvik, T., 2008. Evaluation of identification methods for YLD2004-18p. Int. J. Plast. 24, 2248–2277.

56 Mahesh, S., 2009. A hierarchical model for rate-dependent polycrystals. Int. J. Plast. 25, 752–767.

57 Tjahjanto, D.D., Eisenlohr, P., Roters, F., 2010. A novel grain cluster-based homogenisation scheme. Model. Simul. Mater. Sci. 18, 015006.

58 Kumar, M.A., Mahesh, S., Parameswaran, V., 2011. A 'stack' model of rate-independent polycrystals. Int. J. Plast. 27, 962–981.

59 M'Guil, S., Ahzi, S., Barlat, F., Gracio, J.J., 2011. Microstructural effects on yield surface evolution in cubic metals using the viscoplastic ϕ-model. Int. J. Plast. 27, 102–120.

60 Taylor, G.I., Elam, C.F., 1923. Bakerian lecture: the distortion of an aluminium crystal during a tensile test. Proc. Roy. Soc. A 102 (719), 643–667.

61 Mandel, J., 1965. Généralisation de la théorie de plasticité de W.T. Koiter. Int. J. Solids Struct. 1, 273–295.

62 Hill, R., Rice, J., 1972. Constitutive analysis of elastic-plastic crystals at arbitrary strain. J. Mech. Phys. Solids 20 (6), 401–413.

63 Schmid, E., Boas, W., 1935. Plasticity of Crystals. Chapman and Hall, London.

64 Abdul-Latif, A., Saanouni, K., 1994. Damaged anelastic behavior of FCC polycrystalline metals with micromechanical approach. Int. J. Damage. Mech. 3 (3), 237–259.

65 Saanouni, K., Abdul-Latif, A., 1996. Micromechanical modeling of low cycle fatigue under complex loadings - part I. Theoretical formulation. Int. J. Plast. 12 (9), 1111–1121.

66 Panicaud, B., Saanouni, K., Baczmanski, A., François, M., Cauvin, L., Le Joncour, L., 2011. Theoretical modelling of ductile damage in duplex stainless steels–Comparison between two

micro-mechanical elasto-plastic approaches. Comp. Mater. Sci. 50, 1908–1916.

67 Akpama, H.K., Ben Bettaieb, M., Abed-Meraim, F., 2016. Numerical integration of rate-independent BCC single crystal plasticity models: Comparative study of two classes of numerical algorithms. Int. J. Numer. Meth. Eng. 108 (5), 363–422.

68 Beausir, B., Fundenberger, J-J., 2017. Analysis Tools for Electron and X-ray diffraction, ATEX - software, www.atex-software.eu, Université de Lorraine - Metz.

69 Coleman, T.F., Li, Y., 1996. An interior trust region approach for nonlinear minimization subject to bounds. SIAM Journal on optimization 6 (2), 418–445.

70 Yoon, J.W., Cazacu, O., Mishra, R.K., 2013. Constitutive modeling of AZ31 sheet alloy with application to axial crushing. Mater. Sci. Eng. A. 565, 203–212.

71 Peerlings, R.H.J., Geers, M.G.D., de Borst, R., 2001. A critical comparison of nonlocal and gradient-enhanced softening continua. Int. J. Solids Struct. 38, 7723–7746.

72 Engelen, R., Geers, M.G.D., Baaijens, F., 2003. Nonlocal implicit gradient-enhanced elasto–plasticity for the modelling of softening behaviour. Int. J. Plast. 19, 403–433.

73 Geers, M.G.D., 2004. Finite strain logarithmic hyperelasto-plasticity with softening: A strongly non-local implicit gradient framework. Comput. Methods Appl. Mech. Engrg. 193, 3377–3401.

74 Forest, S., 2016. Nonlinear regularization operators as derived from the micromorphic approach to gradient elasticity, viscoplasticity and damage. Proc. Roy. Soc. A 472, 20150755.

75 Diamantopoulou, E., Liu, W., Labergere, C., Badreddine, H., Saanouni, K., Hu, P., 2017. Micromorphic constitutive equations with damage applied to metal forming. Int. J. Damage Mech. 26 (2), 314–339.

76 Franciosi, P., Zaoui, A., 1991. Crystal hardening and the issue of uniqueness. Int. J. Plast. 7, 295–311.

77 Lipinski, P., Berveiller, M., Reubrez, E., Morreale, J., 1995. Transition theories of elastic-plastic deformation of metallic polycrystals. Arch. Appl. Mech. 65 (5), 291–311.

78 Hill, R., 1972. On constitutive macro-variables for heterogeneous solids at finite strain. Proc. Roy. Soc. A 326 (1565), 131–147.

Appendix A. Some details about FCC single crystals

For the different simulations, single crystals with face-centered cubic (FCC) crystallographic structure are considered. Nevertheless, the proposed numerical methodology remains quite general to be applied to any other crystallographic structure.

A.1. Crystallographic slip systems

In FCC single crystals, plastic deformation results from crystallographic slip along four slip planes $\{111\}$ and three slip directions $\langle 1\bar{1}0 \rangle$, thus leading to twelve CSSs (i.e., $N_s = 12$). The list of vectors $\vec{\underline{\mathbf{b}}}^{\alpha}$ and $\vec{\underline{\mathbf{n}}}^{\alpha}$, measured in the intermediate configuration related to the crystallographic lattice, is enumerated in Table A.1.

Table A.1. The numbering of the CSSs for FCC single crystal.

α	1	2	3	4	5	6	7	8	9	10	11	12
$\sqrt{3}\vec{\underline{\mathbf{n}}}^{\alpha}$	$\begin{Bmatrix}1\\1\\1\end{Bmatrix}$			$\begin{Bmatrix}-1\\1\\1\end{Bmatrix}$			$\begin{Bmatrix}1\\-1\\1\end{Bmatrix}$			$\begin{Bmatrix}1\\1\\-1\end{Bmatrix}$		
$\sqrt{2}\vec{\underline{\mathbf{b}}}^{\alpha}$	$\begin{Bmatrix}1\\-1\\0\end{Bmatrix}$	$\begin{Bmatrix}1\\0\\-1\end{Bmatrix}$	$\begin{Bmatrix}0\\1\\-1\end{Bmatrix}$	$\begin{Bmatrix}1\\1\\0\end{Bmatrix}$	$\begin{Bmatrix}1\\0\\1\end{Bmatrix}$	$\begin{Bmatrix}0\\1\\-1\end{Bmatrix}$	$\begin{Bmatrix}1\\1\\0\end{Bmatrix}$	$\begin{Bmatrix}1\\0\\-1\end{Bmatrix}$	$\begin{Bmatrix}0\\1\\1\end{Bmatrix}$	$\begin{Bmatrix}1\\-1\\0\end{Bmatrix}$	$\begin{Bmatrix}1\\0\\1\end{Bmatrix}$	$\begin{Bmatrix}0\\1\\1\end{Bmatrix}$

A.2. Hardening model

The initial critical shear stress is assumed to be identical for all the CSSs and equal to τ_0. The evolution of the critical shear stresses is described by a nonlinear hardening model, for which the components of the hardening matrix $\mathbf{h}$ are given as follows:

$$\forall \alpha, \upsilon = 1,..., N_s : \quad h^{\alpha\upsilon} = h_0 \, \mathrm{e}^{-b\gamma_\upsilon} a^{\alpha\upsilon}, \tag{A.1}$$

where h_0 and b are hardening parameters and $a^{\alpha\upsilon}$ are the components of the symmetric interaction matrix $\mathbf{a}$. Based on relevant experimental observations for FCC single crystals, Franciosi and Zaoui [76] proposed the interaction matrix provided in Table A.2. In this particular case, the interaction matrix is symmetric and dependent on six interaction coefficients $a_1 - a_6$. This matrix has been used in the current work.

Table A.2. Hardening interaction matrix.

α	1	2	3	4	5	6	7	8	9	10	11	12
1	a_1	a_2	a_2	a_5	a_4	a_5	a_5	a_6	a_3	a_5	a_3	a_6
2		a_1	a_2	a_3	a_5	a_6	a_4	a_5	a_5	a_5	a_6	a_3
3			a_1	a_6	a_5	a_3	a_5	a_3	a_6	a_4	a_5	a_5
4				a_1	a_2	a_2	a_3	a_5	a_6	a_5	a_5	a_4
5					a_1	a_2	a_6	a_5	a_3	a_6	a_3	a_5
6						a_1	a_5	a_4	a_5	a_3	a_6	a_5
7							a_1	a_2	a_2	a_6	a_5	a_3
8								a_1	a_2	a_3	a_5	a_6
9									a_1	a_5	a_4	a_5
10										a_1	a_2	a_2
11											a_1	a_2
12												a_1

Appendix B. Description of the mean-field self-consistent approach

Following the finite strain framework of the self-consistent approach developed in [46, 77], the overall nominal stress rate $\dot{\mathbf{N}}$ is linked to the macroscopic velocity gradient $\mathbf{G}$ through the macroscopic fourth-rank tangent modulus $\mathbb{L}$:

$$\dot{\mathbf{N}} = \mathbb{L} : \mathbf{G}. \tag{B.1}$$

The macroscopic nominal stress rate $\dot{\mathbf{N}}$ is related to the macroscopic Cauchy stress rate $\dot{\boldsymbol{\Sigma}}$ by the following relationship:

$$\dot{\mathbf{N}} = J\,\mathbf{F}^{-1}.\left(\dot{\boldsymbol{\Sigma}} + tr\left(\mathbf{G}\right)\boldsymbol{\Sigma} - \mathbf{G}.\boldsymbol{\Sigma}\right), \tag{B.2}$$

where $\mathbf{F}$ denotes the macroscopic deformation gradient (related to the macroscopic velocity gradient $\mathbf{G}$ by the classical relation $\mathbf{G} = \dot{\mathbf{F}}.\mathbf{F}^{-1}$) and J its determinant. By adopting an updated Lagrangian approach (i.e., $J = 1$ and $\mathbf{F} = \mathbf{I}_2$), Eq. (B.2) reduces to the following form:

$$\dot{\mathbf{N}} = \dot{\boldsymbol{\Sigma}} + tr\left(\mathbf{G}\right)\boldsymbol{\Sigma} - \mathbf{G}.\boldsymbol{\Sigma}. \tag{B.3}$$

On the other hand, macroscopic variables $\mathbf{G}$ and $\dot{\mathbf{N}}$ can be expressed in terms of their microscopic counterparts $\mathbf{g}$ and $\dot{\mathbf{n}}$ by the standard Hill averaging theorem [78]:

$$\mathbf{G} = \frac{1}{V}\int_V \mathbf{g}\left(\vec{\mathbf{x}}\right)\mathrm{d}V, \quad \dot{\mathbf{N}} = \frac{1}{V}\int_V \dot{\mathbf{n}}\left(\vec{\mathbf{x}}\right)\mathrm{d}V, \tag{B.4}$$

where $\vec{\mathbf{x}}$ is the material point coordinates vector in the polycrystalline aggregate and V its volume. Conversely, the microscopic velocity gradient and nominal stress rate are linked to their macroscopic counterparts $\mathbf{G}$ and $\dot{\mathbf{N}}$ by the fourth-rank concentration tensors $\mathbb{A}$ and $\mathbb{B}$:

$$\mathbf{g}\left(\vec{\mathbf{x}}\right) = \mathbb{A}\left(\vec{\mathbf{x}}\right) : \mathbf{G}, \quad \dot{\mathbf{n}}\left(\vec{\mathbf{x}}\right) = \mathbb{B}\left(\vec{\mathbf{x}}\right) : \dot{\mathbf{N}}. \tag{B.5}$$

Similar to the averaging relations given by Eq. (B.4), the macroscopic plastic strain rate $\dot{\mathbf{E}}^p$ can be defined as the average of its microscopic counterpart $\dot{\boldsymbol{\varepsilon}}^p$:

$$\dot{\mathbf{E}}^p = \frac{1}{V}\int_V \dot{\boldsymbol{\varepsilon}}^p\left(\vec{\mathbf{x}}\right)\mathrm{d}V. \tag{B.6}$$

The complete details relating to the expression of $\dot{\boldsymbol{\varepsilon}}^p$ for the single crystal behavior have been given in Section 2.1.

At the single crystal level, a relationship similar to Eq. (B.1) can be derived by combining the microscopic constitutive relations detailed in Section 2.1:

$$\dot{\mathbf{n}}(\vec{\mathbf{x}}) = \ell(\vec{\mathbf{x}}) : \mathbf{g}(\vec{\mathbf{x}}), \tag{B.7}$$

where ℓ is the microscopic fourth-rank tangent modulus. The relation between $\mathbb{L}$ and ℓ can be obtained by combining Eqs. (B.1), (B.4), (B.5) and (B.7):

$$\mathbb{L} = \frac{1}{V}\int_V \ell(\vec{\mathbf{x}}) : \mathbb{A}(\vec{\mathbf{x}}) \mathrm{d}V . \tag{B.8}$$

By following the formulation of the self-consistent approach adopted in [46, 77], we assume that the microscopic mechanical fields are homogeneous over each individual grain. Denoting by $\mathbf{g}^{gr}$ (resp. ℓ^{gr}) the microscopic velocity gradient (resp. tangent modulus) associated with grain gr (with gr ranging from 1 to the total number of grains contained in the RVE Ngr), and using some Green's tensor properties [77], one can prove that the concentration tensor $\mathbb{A}^{gr}$ can be expressed as:

$$\mathbb{A}^{gr} = \left(\mathbb{I}_4 - \mathbb{N}^{gr} : \left(\ell^{gr} - \mathbb{L}\right)\right)^{-1} : \left(\sum_{I=1}^{Ngr} f^I \left(\mathbb{I}_4 - \mathbb{N}^I : \left(\ell^I - \mathbb{L}\right)\right)^{-1}\right)^{-1}, \tag{B.9}$$

where $\mathbb{N}^I$ is the fourth-order interaction tensor for grain I, related to Eshelby's tensor for an ellipsoidal inhomogeneity, and f^I is the volume fraction of grain I, with $\sum_{I=1}^{Ngr} f^I = 1$. Under the assumption of the homogeneity of microscopic mechanical fields, definition (B.8) of the macroscopic tangent modulus $\mathbb{L}$ can be reduced to the following expression:

$$\mathbb{L} = \sum_{gr=1}^{Ngr} f^{gr} \, \ell^{gr} : \mathbb{A}^{gr} . \tag{B.10}$$

Equation (B.10) of the macroscopic tangent modulus $\mathbb{L}$ reveals an implicit character, because the concentration tensor $\mathbb{A}^{gr}$ depends on $\mathbb{L}$ through the expression of $\mathbb{N}^{gr}$ and $\ell^{gr} - \mathbb{L}$ as shown in Eq. (B.9). Therefore, the macroscopic tangent modulus $\mathbb{L}$, which is the main unknown variable in the self-consistent approach, is computed by using the iterative fixed-point method. Further details about the application of this method to solve the self-consistent equations can be found in [45, 49].

Appendix C. Numerical integration of the phenomenological constitutive equations

C.1. Numerical integration scheme

Due to its nonlinear nature, the phenomenological model presented in Sections 2.2.1 and 2.2.2 is solved in an incremental fashion. Over a typical time increment $I^{\Delta}=\left[t_{(n)},t_{(n+1)}\right]$, the resulting constitutive equations are integrated using an implicit backward Euler scheme. This scheme is implemented into ABAQUS/Standard FE code through a user defined material subroutine UMAT. To respect the incremental objectivity, the constitutive equations are integrated in the material corotational frame (for a detailed description of the rotation handling, see [21]). In this frame, the problem is reduced to the determination of the updated Cauchy stress $\boldsymbol{\Sigma}_{(n+1)}$ and internal variables (namely, $R_{(n+1)}$ and $D_{(n+1)}$), knowing the total strain increment $\Delta\mathbf{E}$. In the following appendix, the function ϕ is denoted $\phi\left(\tilde{\boldsymbol{\Sigma}};\bar{E}_p,D\right)$, where the terms $\bar{E}_p$ and D after the semicolon refer to the parametric dependency of ϕ on $\bar{E}_p$ and D (see Section 3.2.4 for explicit expression), and $\tilde{\boldsymbol{\Sigma}}$ is the stress given to the Barlat criterion (Section 2.2.2). The iterative implicit algorithm is based on the elastic prediction-plastic correction methodology, where the trial stress tensor $\boldsymbol{\Sigma}^{*}$ should be firstly computed as follows:

$$\boldsymbol{\Sigma}^{*}_{(n)}=\boldsymbol{\Sigma}_{(n)}+\left(1-D_{(n)}\right)\,\mathbb{C}^{e}:\Delta\mathbf{E}. \tag{C.1}$$

On the basis of this trial stress tensor, the trial yield criterion f^{*} can be determined as follows:

$$f^{*}=\frac{\phi\left(\boldsymbol{\Sigma}^{*}_{(n)};\bar{E}_{p(n)},D_{(n)}\right)}{\sqrt{1-D_{(n)}}}-\left(\Sigma^{Y}+\frac{R_{(n)}}{\sqrt{1-D_{(n)}}}\right). \tag{C.2}$$

If $f^{*}\leq 0$, the behavior is elastic over the current time increment. Then, the updated variables are equal to their trial counterparts. Otherwise, the following developments are used to update the different variables.

The combination of the incremental form of Eq. (14)$_1$ and Eq. (C.1) allows us to determine the stress tensor at the end of the time increment $\boldsymbol{\Sigma}_{(n+1)}$:

$$\boldsymbol{\Sigma}_{(n+1)} = \frac{\left(1-D_{(n+1)}\right)}{\left(1-D_{(n)}\right)}\boldsymbol{\Sigma}^{*}_{(n)} - 2\mu\left(1-D_{(n+1)}\right)\Delta\mathbf{E}^{p}, \tag{C.3}$$

where $\mu = E/2(1+\nu)$ is the Lamé coefficient.

The increment of the plastic strain $\Delta\mathbf{E}^{p}$ is obtained from the incremental form of the plastic flow rule given by Eq. (16):

$$\Delta\mathbf{E}^{p} = \Delta\Lambda\frac{\partial\phi}{\partial\boldsymbol{\Sigma}}\left(\tilde{\boldsymbol{\Sigma}}_{(n+1)};\bar{E}_{p(n+1)},D_{(n+1)}\right) = \frac{\Delta\Lambda}{\sqrt{1-D_{(n+1)}}}\frac{\partial\phi}{\partial\boldsymbol{\Sigma}}\left(\boldsymbol{\Sigma}_{(n+1)};\bar{E}_{p(n+1)},D_{(n+1)}\right). \tag{C.4}$$

The combination of Eqs. (C.4) and (C.3) leads to:

$$\boldsymbol{\Sigma}_{(n+1)} = \frac{\left(1-D_{(n+1)}\right)}{\left(1-D_{(n)}\right)}\boldsymbol{\Sigma}^{*} - 2\mu\Delta\Lambda\sqrt{1-D_{(n+1)}}\frac{\partial\phi}{\partial\boldsymbol{\Sigma}}\left(\boldsymbol{\Sigma}_{(n+1)};\bar{E}_{p(n+1)},D_{(n+1)}\right). \tag{C.5}$$

For the sake of numerical simplicity, let us introduce the function $H\left(\bar{E}^{p}_{(n+1)}\right) = H_1\,\mathrm{e}^{-H_2\,\bar{E}^{p}_{(n+1)}}$. Using this function, the incremental forms of the evolution laws of the state variables D and r can be deduced from Eqs. (17) and (18):

$$D_{(n+1)} = D_{(n)} + \frac{\Delta\Lambda}{\left(1-D_{(n+1)}\right)^{M}}\left\langle\frac{Y_{(n+1)}-Y_0}{S}\right\rangle^{\Theta}, \quad r_{(n+1)} = r_{(n)} + \Delta\Lambda H\left(\bar{E}^{p}_{(n+1)}\right). \tag{C.6}$$

Considering Eqs. $(14)_2$ and $(14)_3$, the thermodynamical forces associated with isotropic hardening and damage can be written in the following incremental forms:

$$\begin{aligned} R_{(n+1)} &= \left(1-D_{(n+1)}\right)Q\,r_{(n+1)} = \frac{\left(1-D_{(n+1)}\right)}{\left(1-D_{(n)}\right)}R_{(n)} + \Delta\Lambda\left(1-D_{(n+1)}\right)Q\,H\left(\bar{E}^{p}_{(n+1)}\right), \\ Y_{(n+1)} &= \frac{1}{2}\frac{\boldsymbol{\Sigma}_{(n+1)}:\mathbb{K}:\boldsymbol{\Sigma}_{(n+1)}}{\left(1-D_{(n+1)}\right)^{2}} + \frac{1}{2}Q\left(r_{(n)} + \Delta\Lambda H\left(\bar{E}^{p}_{(n+1)}\right)\right)^{2}. \end{aligned} \tag{C.7}$$

Then, the main unknowns of the incremental form of the phenomenological constitutive equations are $\boldsymbol{\Sigma}_{(n+1)}$, $\Delta\Lambda$ and $D_{(n+1)}$ (eight scalar unknowns). To determine these unknown, Eqs. $(15)_1$, (C.5) and $(C.6)_1$ should be solved after their combination with Eqs. (C.4) and (C.7):

$$f_{(n+1)} = \frac{\phi\left(\boldsymbol{\Sigma}_{(n+1)};\bar{E}_{p(n+1)},D_{(n+1)}\right)}{\sqrt{1-D_{(n+1)}}} - \left(\Sigma^{Y} + \frac{R_{(n+1)}}{\sqrt{1-D_{(n+1)}}}\right) = 0, \tag{C.8}$$

$$\mathbf{q}_{(n+1)} = \boldsymbol{\Sigma}_{(n+1)} - \frac{\left(1-D_{(n+1)}\right)}{\left(1-D_{(n)}\right)}\boldsymbol{\Sigma}^{*} + 2\mu\,\Delta\Lambda\sqrt{1-D_{(n+1)}}\frac{\partial\bar{\phi}}{\partial\boldsymbol{\Sigma}}\left(\boldsymbol{\Sigma}_{(n+1)};\bar{E}_{p(n+1)},D_{(n+1)}\right)=0, \tag{C.9}$$

$$g_{(n+1)} = D_{(n+1)} - D_{(n)} - \frac{\Delta\Lambda}{\left(1-D_{(n+1)}\right)^{M}}\left\langle\frac{Y_{(n+1)}-Y_0}{S}\right\rangle^{\Theta} = 0. \tag{C.10}$$

The nonlinear equation system made of Eqs. (C.8), (C.9), and (C.10) is solved by the Newton–Raphson scheme, which is implemented into the UMAT. The analytical derivation of the components of the Jacobian matrix associated with this scheme is detailed in Section C.2. A Gauss point is considered to be fully damaged when the value of $D_{(n+1)}$ exceeds 0.9 (at the convergence of the Newton–Raphson scheme). In that case, the time increment of the finite element simulation is divided (up to its minimum value).

C.2. Computation of the tangent matrix required for the Newton–Raphson scheme

To ensure the quadratic convergence of the Newton–Raphson iterative scheme described in Section C.1, the Jacobian matrix corresponding to this method should be accurately computed. To reach this objective, the analytical expressions providing the derivatives of functions f, g, and $\mathbf{q}$ with respect to the main variables $\Delta\Lambda$, D, and $\boldsymbol{\Sigma}$ should be determined. The determination of these expressions will be presented in the following developments where, for sake of simplicity, the anisotropy parameters T_{ij} are assumed to be constant over I^{Δ} and equal to their initial values at $t_{(n)}$. This assumption is reasonable and quite justified considering the fact that these anisotropy parameters slowly evolve over the time increment. Consequently, the derivatives of parameters T_{ij} with respect to variables $\boldsymbol{\Sigma}$, $\Delta\Lambda$ and D are obviously equal to 0.

C.2.1. Derivatives with respect to $\Delta\Lambda$

The derivatives of functions f, g, and $\mathbf{q}$ with respect to $\Delta\Lambda$ read:

$$\frac{\partial f}{\partial\Delta\Lambda} = -\frac{1}{\sqrt{1-D}}\frac{\partial R}{\partial\Delta\Lambda} = -\sqrt{1-D}\,Q\,H\left(\bar{E}^{p}\right), \tag{C.11}$$

$$\frac{\partial g}{\partial\Delta\Lambda} = -\frac{1}{\left(1-D\right)^{M}}\left\langle\frac{Y-Y_0}{S}\right\rangle^{\Theta} - \frac{\Theta\,\Delta\Lambda}{S\,\left(1-D\right)^{M}}\frac{\partial Y}{\partial\Delta\Lambda}\left\langle\frac{Y-Y_0}{S}\right\rangle^{\Theta-1}, \tag{C.12}$$

$$\frac{\partial\mathbf{q}}{\partial\Delta\Lambda} = 2\mu\,\sqrt{1-D}\frac{\partial\bar{\phi}}{\partial\boldsymbol{\Sigma}}, \tag{C.13}$$

with the derivative $\partial Y / \partial\Delta\Lambda$ involved in Eq. (C.12) given by the following equation:

$$\frac{\partial Y}{\partial \Delta\lambda} = Q\,H\left(\bar{E}^p\right)\left(r + \Delta\lambda\, H\left(\bar{E}^p\right)\right). \tag{C.14}$$

C.2.2. Derivatives with respect to D

The derivatives of functions f, g, and $\mathbf{q}$ with respect to D read:

$$\frac{\partial f}{\partial D} = \frac{\phi - R}{2(1-D)^{3/2}} - \frac{1}{\sqrt{1-D}}\frac{\partial R}{\partial D}, \tag{C.15}$$

$$\frac{\partial g}{\partial D} = 1 - \frac{M\,\Delta\lambda}{(1-D)^{M+1}}\left\langle\frac{Y - Y_0}{S}\right\rangle^{\Theta} - \frac{\Theta\,\Delta\lambda}{S(1-D)^{M}}\frac{\partial Y}{\partial D}\left\langle\frac{Y - Y_0}{S}\right\rangle^{\Theta-1}, \tag{C.16}$$

$$\frac{\partial \mathbf{q}}{\partial D} = \frac{1}{(1-D)}\boldsymbol{\Sigma}^{*} - \frac{\mu\Delta\lambda}{\sqrt{1-D}}\frac{\partial \bar{\phi}}{\partial \boldsymbol{\Sigma}}, \tag{C.17}$$

with the derivatives $\partial R / \partial D$ and $\partial Y / \partial D$, used in Eqs. (C.15) and (C.16), respectively, having the following expressions:

$$\frac{\partial R}{\partial D} = \frac{-1}{(1-D)}R - \Delta\lambda\, Q\, H\left(\bar{E}^p\right), \tag{C.18}$$

$$\frac{\partial Y}{\partial D} = \frac{\boldsymbol{\Sigma} : \mathbb{K} : \boldsymbol{\Sigma}}{(1-D)^3}. \tag{C.19}$$

C.2.3. Derivatives with respect to $\boldsymbol{\Sigma}$

The derivatives of functions f, g, and $\mathbf{q}$ with respect to $\boldsymbol{\Sigma}$ read:

$$\frac{\partial f}{\partial \boldsymbol{\Sigma}} = \frac{1}{\sqrt{1-D}}\frac{\partial \bar{\phi}}{\partial \boldsymbol{\Sigma}}, \tag{C.20}$$

$$\frac{\partial g}{\partial \boldsymbol{\Sigma}} = -\frac{\Theta\,\Delta\lambda}{S(1-D)^{M}}\frac{\partial Y}{\partial \boldsymbol{\Sigma}}\left\langle\frac{Y - Y_0}{S}\right\rangle^{\Theta-1}, \tag{C.21}$$

$$\frac{\partial \mathbf{q}}{\partial \boldsymbol{\Sigma}} = \mathbb{I}_4 + 2\mu\,\Delta\lambda\sqrt{1-D}\,\frac{\partial^2 \bar{\phi}}{\partial \boldsymbol{\Sigma}^2}, \tag{C.22}$$

with the derivative $\partial Y / \partial \boldsymbol{\Sigma}$ implied in Eq. (C.21) defined as follows:

$$\frac{\partial Y}{\partial \boldsymbol{\Sigma}} = \frac{\mathbb{K} : \boldsymbol{\Sigma}}{(1-D)^2}. \tag{C.23}$$

C.2.4. First and second order derivatives of ϕ with respect to $\boldsymbol{\Sigma}$

The analytical expression of $\partial\phi/\partial\boldsymbol{\Sigma}$ is needed in Eq. (C.20). To obtain this expression, we introduce tensors $\boldsymbol{\mathcal{G}}_i$ $(i=1,...,3)$, which allow decomposing tensor $\mathbf{S}=\mathbb{T}:\boldsymbol{\Sigma}$ as follows:

$$\mathbf{S}=\mathbb{T}:\boldsymbol{\Sigma}=\sum_{i=1}^{3}S_i\,\boldsymbol{\mathcal{G}}_i. \tag{C.24}$$

Then, one can demonstrate that:

$$\frac{\partial\phi}{\partial\boldsymbol{\Sigma}}=\sum_{i=1}^{3}\frac{\partial\phi}{\partial S_i}\frac{\partial S_i}{\partial\boldsymbol{\Sigma}}=\sum_{i=1}^{3}\frac{\partial\phi}{\partial S_i}\frac{\partial S_i}{\partial\mathbf{S}}:\frac{\partial\mathbf{S}}{\partial\boldsymbol{\Sigma}}=\sum_{i=1}^{3}\frac{\partial\phi}{\partial S_i}\mathbb{T}:\boldsymbol{\mathcal{G}}_i, \tag{C.25}$$

and

$$\frac{\partial\phi}{\partial S_i}=\left(\sum_{r\neq i}\operatorname{sgn}\left(S_i-S_r\right)\left|S_i-S_r\right|^{A-1}\right)\phi^{1-A}. \tag{C.26}$$

Similarly to Eq. (C.25), we can directly determine the expression of the derivative $\partial\underline{\phi}/\partial\boldsymbol{\Sigma}$:

$$\frac{\partial\underline{\phi}}{\partial\boldsymbol{\Sigma}}=\sum_{i=1}^{3}\frac{\partial\underline{\phi}}{\partial\underline{S}_i}\frac{\partial\underline{S}_i}{\partial\boldsymbol{\Sigma}}=\sum_{i=1}^{3}\frac{\partial\underline{\phi}}{\partial\underline{S}_i}\frac{\partial\underline{S}_i}{\partial\underline{\mathbf{S}}}:\frac{\partial\underline{\mathbf{S}}}{\partial\boldsymbol{\Sigma}}=\sum_{i=1}^{3}\frac{\partial\underline{\phi}}{\partial\underline{S}_i}\underline{\mathbb{T}}:\boldsymbol{\mathcal{G}}_i. \tag{C.27}$$

As stated in the identification procedure (see Section 3.2.5), the transformation matrix $\underline{\mathbb{T}}$ is assumed to be identically equal to $\mathbb{T}$. Under this assumption, Eq. (C.27) can be rewritten as follows:

$$\frac{\partial\underline{\phi}}{\partial\boldsymbol{\Sigma}}=\sum_{i=1}^{3}\frac{\partial\underline{\phi}}{\partial S_i}\frac{\partial S_i}{\partial\boldsymbol{\Sigma}}=\sum_{i=1}^{3}\frac{\partial\underline{\phi}}{\partial S_i}\frac{\partial S_i}{\partial\mathbf{S}}:\frac{\partial\mathbf{S}}{\partial\boldsymbol{\Sigma}}=\sum_{i=1}^{3}\frac{\partial\underline{\phi}}{\partial S_i}\mathbb{T}:\boldsymbol{\mathcal{G}}_i, \tag{C.28}$$

where $\partial\underline{\phi}/\partial S_i$ is given by a relation very similar to Eq. (C.26):

$$\frac{\partial\underline{\phi}}{\partial S_i}=\left(\sum_{r\neq i}\operatorname{sgn}\left(S_i-S_r\right)\left|S_i-S_r\right|^{\underline{A}-1}\right)\underline{\phi}^{1-\underline{A}}. \tag{C.29}$$

The second derivative $\partial^2\underline{\phi}/\partial\boldsymbol{\Sigma}^2$ involved in Eq. (C.22) is obtained by taking the derivative of Eq. (C.27) with respect to $\boldsymbol{\Sigma}$:

$$
\begin{aligned}
\frac{\partial^2 \underline{\phi}}{\partial \boldsymbol{\Sigma}^2} &= \frac{\partial}{\partial \boldsymbol{\Sigma}}\left[\sum_{i=1}^{3} \frac{\partial \underline{\phi}}{\partial S_i}\mathbb{T}:\boldsymbol{\mathcal{G}}_i\right] \\
&= \sum_{i=1}^{3} \frac{\partial^2 \underline{\phi}}{\partial \boldsymbol{\Sigma}\partial S_i} \otimes \left(\mathbb{T}:\boldsymbol{\mathcal{G}}_i\right) + \sum_{i=1}^{3} \frac{\partial \underline{\phi}}{\partial S_i}\mathbb{T}:\frac{\partial \boldsymbol{\mathcal{G}}_i}{\partial \boldsymbol{\Sigma}} \\
&= \sum_{i=1}^{3} \frac{\partial}{\partial S_i}\left[\frac{\partial \underline{\phi}}{\partial \boldsymbol{\Sigma}}\right] \otimes \left(\mathbb{T}:\boldsymbol{\mathcal{G}}_i\right) + \sum_{i=1}^{3} \frac{\partial \underline{\phi}}{\partial S_i}\,\mathbb{T}:\frac{\partial \boldsymbol{\mathcal{G}}_i}{\partial \mathbf{S}}:\frac{\partial \mathbf{S}}{\partial \boldsymbol{\Sigma}} \\
&= \sum_{i=1}^{3} \frac{\partial}{\partial S_i}\left[\sum_{r=1}^{3} \frac{\partial \underline{\phi}}{\partial S_r}\mathbb{T}:\boldsymbol{\mathcal{G}}_r\right] \otimes (\mathbb{T}:\boldsymbol{\mathcal{G}}_i) + \sum_{i=1}^{3} \frac{\partial \underline{\phi}}{\partial S_i}\mathbb{T}:\frac{\partial \boldsymbol{\mathcal{G}}_i}{\partial \mathbf{S}}:\mathbb{T} \\
&= \sum_{i=1}^{3}\sum_{r=1}^{3} \frac{\partial^2 \underline{\phi}}{\partial S_i \partial S_r}\left(\mathbb{T}:\boldsymbol{\mathcal{G}}_r\right) \otimes \left(\mathbb{T}:\boldsymbol{\mathcal{G}}_i\right) + \sum_{i=1}^{3} \frac{\partial \underline{\phi}}{\partial S_i}\mathbb{T}:\frac{\partial \boldsymbol{\mathcal{G}}_i}{\partial \mathbf{S}}:\mathbb{T}
\end{aligned}
\tag{C.30}
$$

and

$$
\frac{\partial^2 \underline{\phi}}{\partial S_i\, \partial S_r} = \frac{(1-\underline{A})}{\underline{\phi}}\frac{\partial \underline{\phi}}{\partial S_i}\frac{\partial \underline{\phi}}{\partial S_r} + (\underline{A}-1)\left(\delta_{ir}\sum_{p\neq i}|\,S_p - S_i\,|^{\underline{A}-2} - |\,S_r - S_i\,|^{\underline{A}-2}\right)\underline{\phi}^{1-\underline{A}}. \tag{C.31}
$$

C.3. Computation of the elastoplastic consistent tangent operator

At the convergence of the Newton–Raphson scheme used to integrate the constitutive equations, the elastoplastic consistent tangent operator $\mathbb{C}^{ep}$ should be computed to ensure the quadratic convergence of the ABAQUS global Newton–Raphson implicit iterative scheme. This tangent operator is defined as:

$$
\mathbb{C}^{ep} = \frac{\partial \Delta \boldsymbol{\Sigma}}{\partial \Delta \mathbf{E}}. \tag{C.32}
$$

The combination of Eqs. (C.1), (C.3), and (C.4) gives:

$$
\Delta \boldsymbol{\Sigma} = (1-D)\mathbb{C}^e : \Delta \mathbf{E} - 2\mu\sqrt{1-D}\,\Delta \Lambda \frac{\partial \phi}{\partial \boldsymbol{\Sigma}}. \tag{C.33}
$$

Using Eqs. (C.32) and (C.33), and considering the derivatives of all the terms depending on the total strain increment $\Delta \mathbf{E}$, the expression of the tangent operator becomes:

$$
\mathbb{C}^{ep} = \mathbb{S}^{-1} : \left[(1-D)\mathbb{C}^e - \frac{\alpha_\lambda}{\alpha_D}\left(\mathbb{C}^e : \Delta \mathbf{E}\right) \otimes \frac{\partial \Delta \Lambda}{\partial \Delta \mathbf{E}} + \left(\frac{\mu \Delta \Lambda}{\sqrt{1-D}}\frac{\alpha_\lambda}{\alpha_D} - 2\mu\sqrt{1-D}\right)\frac{\partial \underline{\phi}}{\partial \boldsymbol{\Sigma}} \otimes \frac{\partial \Delta \Lambda}{\partial \Delta \mathbf{E}}\right], \tag{C.34}
$$

with the fourth-rank tensor $\mathbb{S}$ defined as:

$$
\mathbb{S} = \mathbb{I}_4 + \left[\mathbb{C}^e : \Delta \mathbf{E} + \frac{\mu \Delta \Lambda}{\sqrt{1-D}}\frac{\partial \underline{\phi}}{\partial \boldsymbol{\Sigma}}\right] \otimes \frac{\boldsymbol{\alpha}_{\boldsymbol{\Sigma}}}{\alpha_D} \quad \text{where} \quad \boldsymbol{\alpha}_{\boldsymbol{\Sigma}} = \frac{\Delta \Lambda}{(1-D)^M}\left(\frac{Y - Y_0}{S}\right)^{\Theta - 1}\frac{\Theta}{S}\frac{\mathbb{K} : \boldsymbol{\Sigma}}{(1-D)^2}, \tag{C.35}
$$

and

$$\frac{\partial \Delta \Lambda}{\partial \Delta \mathbf{E}} = \sqrt{1-D}\,\frac{\dfrac{\partial \phi}{\partial \boldsymbol{\Sigma}}}{\dfrac{\partial \phi}{\partial \boldsymbol{\Sigma}} : \dfrac{\partial \phi}{\partial \boldsymbol{\Sigma}}}. \tag{C.36}$$

Scalars α_λ and α_D introduced in Eqs. (C.34) and (C.35) are given by the following expressions:

$$\begin{aligned}
\alpha_\lambda &= \frac{1}{(1-D)^M}\left(\frac{Y-Y_0}{S}\right)^{\Theta} + \frac{\Delta \Lambda}{(1-D)^M}\left(\frac{Y-Y_0}{S}\right)^{\Theta-1}\frac{\Theta}{S} Q\, H\left(\bar{E}^p\right)\left(r + \Delta\lambda\, H\left(\bar{E}^p\right)\right), \\
\alpha_D &= 1 + \frac{M\,\Delta \Lambda}{(1-D)^{M+1}}\left(\frac{Y-Y_0}{S}\right)^{\Theta} + \frac{\Delta \Lambda}{(1-D)^M}\left(\frac{Y-Y_0}{S}\right)^{\Theta-1}\frac{\Theta}{S}\frac{\boldsymbol{\Sigma} : \mathbb{K} : \boldsymbol{\Sigma}}{(1-D)^3}.
\end{aligned} \tag{C.37}$$